



LJMU Research Online

Gkantou, M, Bock, M and Theofanous, M

Design of stainless steel cross-sections with outstand elements under stress gradients

<http://researchonline.ljmu.ac.uk/id/eprint/14227/>

Article

Citation (please note it is advisable to refer to the publisher's version if you intend to cite from this work)

Gkantou, M, Bock, M and Theofanous, M (2021) Design of stainless steel cross-sections with outstand elements under stress gradients. Journal of Constructional Steel Research, 179. ISSN 0143-974X

LJMU has developed **LJMU Research Online** for users to access the research output of the University more effectively. Copyright © and Moral Rights for the papers on this site are retained by the individual authors and/or other copyright owners. Users may download and/or print one copy of any article(s) in LJMU Research Online to facilitate their private study or for non-commercial research. You may not engage in further distribution of the material or use it for any profit-making activities or any commercial gain.

The version presented here may differ from the published version or from the version of the record. Please see the repository URL above for details on accessing the published version and note that access may require a subscription.

For more information please contact researchonline@ljmu.ac.uk

<http://researchonline.ljmu.ac.uk/>

Design of stainless steel cross-sections with outstand elements under stress gradients

Michaela Gkantou^a, Marina Bock^b, Marios Theofanous^c

^a School of Civil Engineering and Built Environment, Faculty of Engineering and Technology, Liverpool John Moores University, L3 3AF, UK, Email: m.gkantou@ljmu.ac.uk

^b School of Architecture and Built Environment, Faculty of Science and Engineering, University of Wolverhampton, WV1 1LY, UK, Email: marina.bock@wlv.ac.uk

^c Department of Civil Engineering, School of Engineering, University of Birmingham, B15 2TT, UK, Email: m.theofanous@bham.ac.uk

Abstract

A significant amount of research has been reported on stainless steel tubular sections, while studies on I- and C-sections remain relatively limited. This paper presents a comprehensive numerical study on the response of stainless steel I- and C-sections subjected to minor axis bending, with outstand flanges subjected to stress gradients. Numerical models are developed and validated against reported test data on austenitic stainless steel sections under minor axis bending. Subsequently, parametric studies using standardised material properties on austenitic, duplex and ferritic stainless steel grades, covering a wide variety of cross-section slendernesses, are carried out to expand the structural performance data. The results are used to assess the applicability of the Eurocode slenderness limits, revealing that the Class limit 3 for outstand flanges under stress gradient is overly conservative. Moreover, Eurocode underestimates the predicted bending strengths, whereas the level of accuracy and consistency improves for stocky sections, when the Continuous Strength Method is used. Aiming to address the lack of accuracy and consistency in the design predictions of slender sections, particular focus is placed on their performance. It is demonstrated that outstand elements under stress gradients exhibit significant inelastic behaviour after the compression flanges have locally buckled. Inelastic buckling behaviour is not considered in current design guidance, thus resulting in overly conservative and fundamentally incorrect strength predictions. An alternative design method based on the plastic effective width concept is proposed for slender stainless steel I- and C-sections in minor axis bending, which leads to more favourable and less scattered strength predictions.

Keywords: Stainless Steel; Local buckling; Outstand Elements; Numerical Modelling; Design; Plastic effective width.

1 INTRODUCTION

Stainless steels are receiving increasing attention in modern structural engineering applications, due to their advantageous features, such as aesthetic appearance, high strength and

35 considerable ductility. An important benefit is that they offer excellent corrosion resistance
36 which leads to low maintenance costs and thus to a reduced life cycle cost that offsets the high
37 initial material cost. Numerous studies were performed on stainless steel structural components
38 in order to examine their ultimate performance and assess the applicability of codified design
39 provisions. Tubular sections including rectangular, square, circular and oval hollow sections
40 have been extensively studied. Examples of reported research include stub [1, 2] and slender
41 columns [3, 4], beams [5, 6], continuous beams [7, 8] and beam-columns [9, 10]. Even though
42 the behaviour of cross-sections comprising internal elements has been well understood,
43 research on cross-sections with outstand flanges remains relatively limited. Experiments have
44 been carried out to examine the behaviour of I-section stub and slender columns [11], major
45 [12] and minor axis [13] bending. In addition, research on C-sections, investigating the flexural
46 response [14] and cross-sectional performance under combined compression and bending [15,
47 16] has also been reported.

48 The aim of this study is to generate structural performance data and gain a better
49 understanding of the structural behaviour of stainless steel sections employing outstand
50 elements subjected to bending. To achieve this, the paper focusses on the ultimate performance
51 of I- and C-sections under minor axis bending. Ultimately, the aim is also to assess codified
52 design provisions for cross-sectional resistance of outstand elements subjected to stress
53 gradients. Section 2 begins with a brief description of the reported test data on austenitic
54 stainless steel I- and C-sections subjected to minor axis bending [13, 14] upon which a
55 numerical model was developed and validated. Using standardised material properties for
56 austenitic, ferritic and duplex stainless steels [17], a parametric study is subsequently conducted
57 in Section 3. The numerically obtained flexural strengths are used to assess design predictions
58 in Section 4. Particular focus is placed on slender sections and design recommendations in line
59 with the observed response are made. Conclusions and design recommendations are
60 summarised in Section 5.

61 **2 NUMERICAL MODELLING**

62 Numerical models were generated using the general purpose finite element (FE) software
63 Abaqus [18]. The FE models were validated against reported experimental results on stainless
64 steel I-sections [13] and C-sections [14]. A brief description of the experimental programme is
65 presented in Section 2.1, whilst Sections 2.2 and 2.3 provide information on the development
66 and validation of the FE models, respectively.

67 **2.1 Selected test data**

68 Experimental studies on austenitic stainless steel beams tested in the 3-point bending and 4-
69 point bending configuration have been reported in [13] and [14] for I- and C-sections,
70 respectively. Since the present study focusses on structural components tested under minor axis
71 bending, only relevant test data from [13, 14] are utilised. Hence, for channel sections emphasis
72 was placed on the case of minor axis bending with the flange tips in compression which is
73 designated as orientation “u” in [14]. The tested sections were laser welded and had sharp edges
74 and corners as shown in Figure 1, where the notation of the section geometry adopted herein is
75 also included. The dimensions and the designations of the tested specimens along with the

76 measured imperfections w_o and the ultimate experimental moments ($M_{u,Exp}$) reported in [13, 14]
77 are summarised for reference in Table 1. The slenderness parameter $c_f/(t_f \epsilon)$ where
78 $\epsilon = [(235/f_y)/(E/210000)]^{0.5}$, and c_f is the flat part of the flange (i.e., $b/2 - t_w/2$ for I-sections and $b -$
79 t_w for C-sections) is also included. The plate slenderness of the flange ($\bar{\lambda}_p$) and cross-sectional
80 slenderness ($\bar{\lambda}_{cs}$) calculated according to Equations (5) and (7) of this paper are also provided in
81 Table 1. Even though the subsequent parametric study discussed in Section 3 will focus only
82 on beams loaded in the 4-point configuration, it was decided to base the ability of the FE models
83 to accurately replicate the experimental response on all relevant available test data under minor
84 axis bending. Therefore, both 4-point and 3-point bending tests were modelled.
85

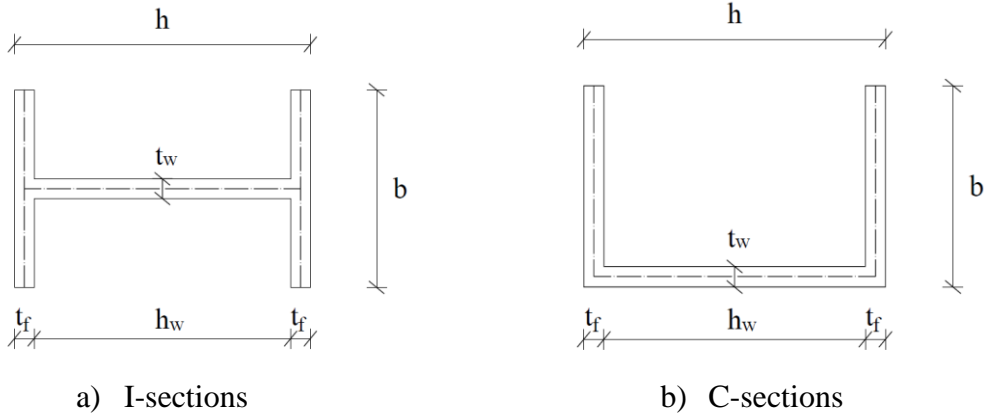


Figure 1: Cross-section geometry and notation of specimens.

Table 1: Summary of test results [13, 14].

Specimen	Section type	Load case	Length (mm)	b (mm)	h (mm)	t_f (mm)	t_w (mm)	w_o (mm)	$c_f/(t_f \epsilon)$	$\bar{\lambda}_p$	$\bar{\lambda}_{cs}$	$M_{u,Exp}$ (kNm)
B3	I-sections	4-point	1100	67.99	101.24	5.05	5.07	0.22 ($t_f/23$)	6.42	0.31	0.25	4.44
B7			1100	82.26	160.63	11.96	10.04	0.16 ($t_f/75$)	3.43	0.18	0.14	17.85
B11			900	50.61	50.21	4.10	4.04	0.23 ($t_f/18$)	6.39	0.34	0.28	2.06
B13			1700	133.92	205.21	7.91	5.97	0.11 ($t_f/72$)	9.24	0.49	0.33	27.69
B15			1500	110.51	219.36	8.97	6.09	0.15 ($t_f/60$)	6.70	0.36	0.24	20.93
B19			1100	75.90	150.77	9.90	6.96	0.16 ($t_f/62$)	3.83	0.20	0.15	11.91
B4	I-sections	3-point	1100	67.50	102.00	4.80	4.80	0.22 ($t_f/22$)	6.73	0.32	0.26	5.91
B8			1100	82.58	160.37	11.78	9.83	0.16 ($t_f/74$)	3.51	0.19	0.14	24.65
B12			1100	50.47	50.55	3.96	3.98	0.23 ($t_f/17$)	6.60	0.35	0.29	2.50
B14			1700	133.97	205.30	7.88	6.01	0.11 ($t_f/72$)	9.27	0.49	0.33	30.48
B16			1100	110.47	219.46	8.94	6.10	0.15 ($t_f/60$)	6.71	0.36	0.25	28.05
B20			1100	75.80	149.93	9.97	7.01	0.16 ($t_f/62$)	3.79	0.19	0.15	15.59
C40×40×5×5	C-sections	4-point	750	39.88	39.99	4.84	4.61	0.48 ($t_f/10$)	9.09	0.42	0.30	2.95
C100×50×4×4			750	49.99	100.28	3.97	3.96	0.72 ($t_f/6$)	14.10	0.66	0.46	3.08
C100×50×6×9			750	49.45	100.35	8.82	5.93	0.38 ($t_f/23$)	6.08	0.29	0.20	7.48
C40×40×5×5	C-sections	3-point	750	39.95	39.94	4.78	4.64	0.48 ($t_f/10$)	9.22	0.43	0.31	3.19
C100×50×4×4			750	49.96	100.97	3.94	3.85	0.72 ($t_f/5$)	14.21	0.66	0.47	3.61
C100×50×6×9			750	49.51	100.35	8.84	5.96	0.38 ($t_f/23$)	5.90	0.28	0.20	9.23

89 2.2 Modelling assumptions

90 The four-noded shell element with reduced integration and finite membrane strains S4R has
 91 been adopted in the development of the FE models, since this type of element has been widely
 92 and successfully used in similar applications [2-6, 8]. The models were based on cross-sectional
 93 centreline dimensions. Upon execution of an initial mesh convergence study, the models were
 94 discretised with a uniform mesh of an element size approximately equal to the plate thickness,
 95 as this mesh size resulted in the optimal compromise between accuracy and computational cost.
 96 The developed FE model for a beam loaded in the 4-point bending configuration along with the
 97 applied boundary conditions is shown in Figure 2. The 3-point FE models were similar to the
 98 models shown in Figure 2, but with one load only applied at the mid-span of the beam.
 99 Kinematic coupling constraints were employed at the supports and at the points of load
 100 application to simulate the plates used in the test to eliminate any local bearing failure.
 101 Symmetry in terms of geometry, boundary conditions, applied loads and failure modes was
 102 exploited by modelling only a quarter of the geometry and applying suitable boundary
 103 conditions as shown in Figure 2, thereby the computational cost was significantly reduced
 104 without compromising accuracy.

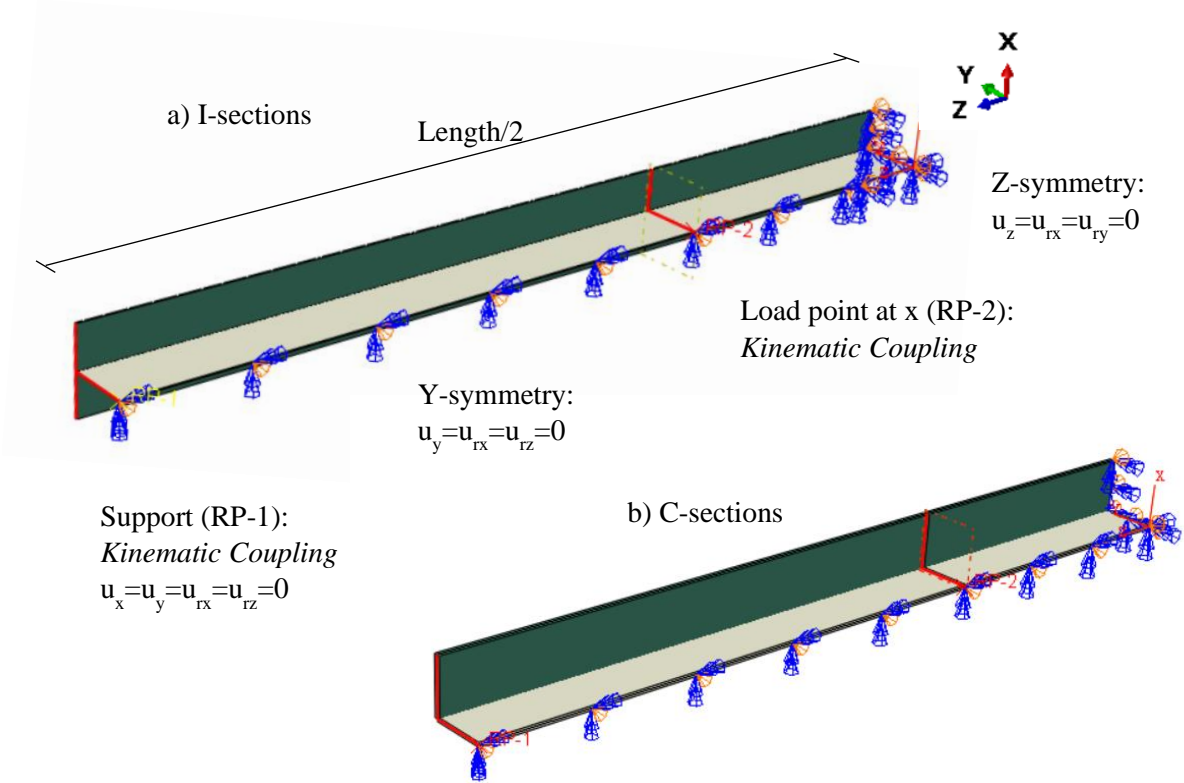
105 Material nonlinearity was modelled based on the von Mises yield criterion with isotropic
 106 hardening. The material behaviour of each section, as determined from reported tensile coupon
 107 test data [13, 14], with the relevant approximations of the adopted stress-strain curves, are
 108 shown in Figure 3. These curves, which are defined in terms of engineering stress and strain,
 109 were converted into true stress σ_{true} and logarithmic plastic strain ε_{ln}^{pl} and incorporated into the
 110 FE model by using Eqs. (1)-(2), where σ_{eng} and ε_{eng} are the engineering stress and strain
 111 respectively and E is the Young's modulus.

$$\sigma_{true} = \sigma_{eng} (1 + \varepsilon_{eng}) \quad (1)$$

$$\varepsilon_{ln}^{pl} = \ln(1 + \varepsilon_{eng}) - \sigma_{true} / E \quad (2)$$

112 In line with past studies [5], residual stresses were not explicitly modelled. However, the
 113 effect of residual stresses on the ultimate capacity was implicitly considered through the
 114 incorporation of the initial geometric imperfections, allowing a successful validation of the
 115 model, as is presented in the following section. This approach is justified, given that both
 116 geometric imperfections and residual stresses lead to an earlier loss of stiffness and precipitate
 117 buckling. A nonlinear static analysis using the modified Riks procedure and taking into
 118 consideration material and geometric nonlinearities [18] was subsequently performed to
 119 determine the response of I- and C-sections subjected to minor axis bending. Initial geometric
 120 imperfections in the form of the buckling mode shape corresponding to the lowest symmetric
 121 elastic critical buckling load were incorporated in the models as discussed hereafter.

122



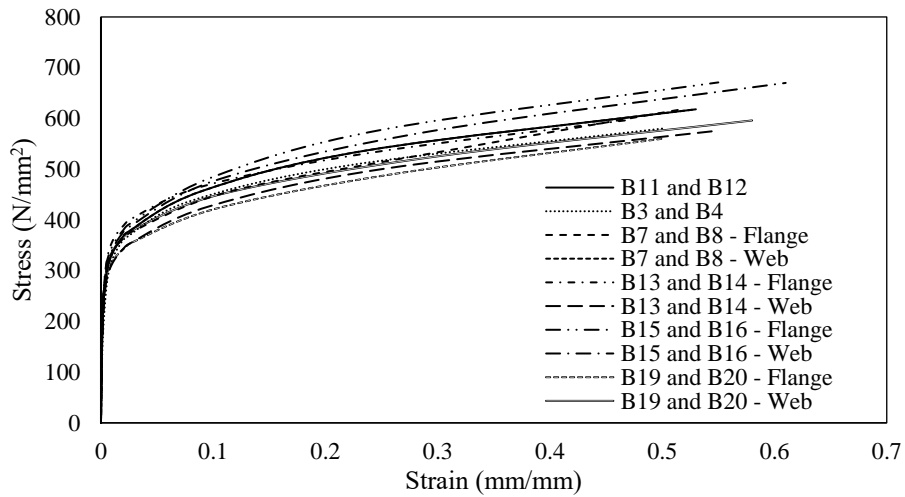
123

124

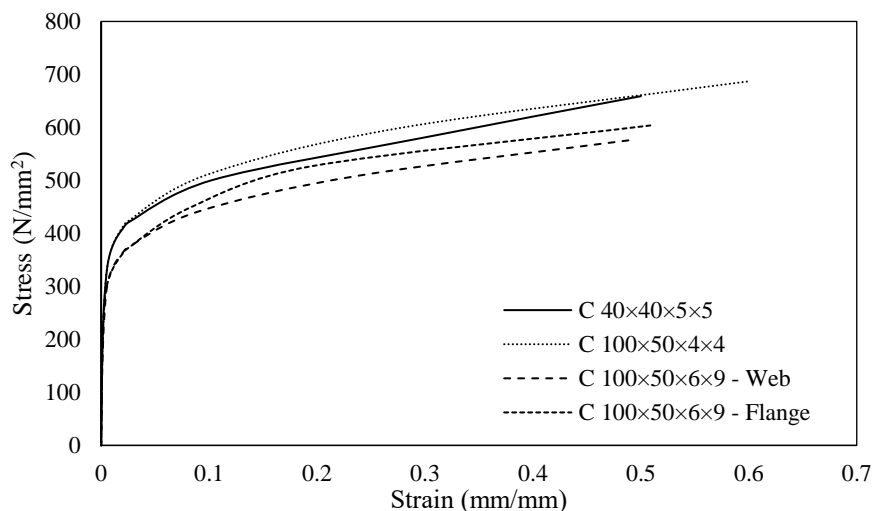
Figure 2: Geometrical modelling and applied boundary conditions.

125

126



a) I-sections [13]



b) C-sections [14]

127 Figure 3: Material properties applied in the FE Models.

128

129 2.3 Model Validation

130 In order to evaluate the accuracy of the finite element models, the numerical results were
 131 compared with the experimental ones reported in [13, 14]. Table 2 shows the ratio of
 132 experimental over FE ultimate moment ($M_{u,Exp}/M_{u,FE}$) for varying geometric imperfection
 133 amplitudes. Five imperfection magnitudes were considered, i.e., the measured w_o values [13,
 134 14], three fractions of the flange thickness ($t_f/100$, $t_f/50$ and $t_f/10$) and a fraction of the flange
 135 width ($b/200$). It can be observed that the initial imperfection magnitude does not have a
 136 significant effect on the ultimate performance of the beams, especially for I-sections. Overall,
 137 a fairly good agreement between the test and numerical data has been obtained with mean
 138 values close to unity and relatively low coefficient of variation (COV). Best agreement was
 139 found to be achieved for the imperfection magnitude $b/200$. The fact that measured imperfection
 140 amplitudes did not provide the most accurate moment predictions could be related with
 141 inaccuracies in the experimental measurement of the imperfections and with the fact that the
 142 measured imperfection pattern is not represented correctly by the buckling mode shapes
 143 obtained from eigenvalue buckling analysis. Most importantly, the maximum imperfection
 144 value measured over a representative length of each section was adopted as a representative
 145 imperfection amplitude for all specimens employing the same cross-section, whilst it is very
 146 likely that in the region of failure the actual imperfection amplitude was smaller than the
 147 maximum measured one. Typical experimental and numerical failure modes are shown in
 148 Figure 4, demonstrating a close agreement between experimental and numerical response in
 149 terms of the obtained failure mode.

150 Key numerical results have been extracted and the moment normalised by the plastic
 151 moment resistance (M/M_{pl}) was plotted against the normalised curvature (k/k_{pl}) for models
 152 loaded in the 4-point bending configuration (or the normalised rotation (θ/θ_{pl}) for 3-point
 153 bending configuration). The plastic curvature k_{pl} and the plastic rotation θ_{pl} is defined as the
 154 elastic part of the total curvature (or rotation) at M_{pl} and determined by $k_{pl}=M_{pl}/EI$ and

155 $\theta_{pl}=M_{pl}L/4EI$ where I is the second moment of area of the cross-section and L is the span.
 156 Typical experimental and numerical moment-curvature (or moment-rotation) responses for the
 157 imperfection magnitude $b/200$ are shown in Figure 5 in a nondimensional format,
 158 demonstrating that the numerical simulations closely matched the experimental response
 159 throughout the full range of deformations. Similar to some tests reported in [13], several
 160 numerical models of stocky I-sections (with $c_f/(t_f\epsilon)$ lower than 7) exhibited a pronounced loss
 161 of stiffness with increasing loading, but no failure occurred, i.e., the recorded moment-curvature
 162 behaviour displayed no maximum. For cases where no failure was observed, the numerical
 163 maximum moment was taken as the moment corresponding to the maximum deformation (in
 164 terms of curvature and rotation for 4-point and 3-point bending respectively) recorded during
 165 testing.

166 Table 2: Comparison between experimental [13, 14] and FE ultimate moments.

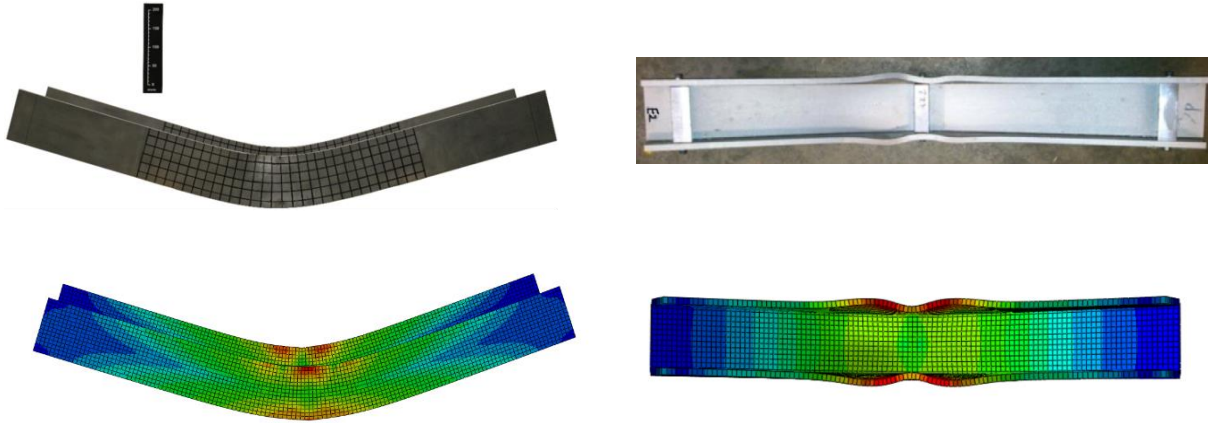
Specimen	Section type	Load case	$M_{u,Exp} / M_{u,FE}$				
			Imperfection Amplitude				
			w_o	$t_f/100$	$t_f/50$	$t_f/10$	$b/200$
B3	I-sections	4-point	1.08	1.08	1.08	1.08	1.08
B7			1.00	0.99	1.00	0.98	0.99
B11			1.14	1.14	1.14	1.14	1.14
B13			1.08	1.08	1.08	1.00	1.01
B15			1.06	1.06	1.06	1.06	1.06
B19			1.06	1.06	1.06	1.06	1.06
B4	I-sections	3-point	0.95	0.95	0.95	0.95	0.95
B8			0.98	0.98	0.98	0.98	0.98
B12			1.03	1.10	1.10	0.98	1.02
B14			1.14	1.14	1.14	1.07	1.08
B16			1.03	1.03	1.04	1.04	1.03
B20			1.11	1.11	1.11	1.12	1.11
C40×40×5×5	C-sections	4-point	1.32	1.17	1.19	1.32	1.19
C100×50×4×4			1.11	0.95	0.97	1.05	1.01
C100×50×6×9			1.06	1.08	1.07	1.05	1.07
C40×40×5×5	C-sections	3-point	1.14	1.04	1.06	1.14	0.99
C100×50×4×4			1.12	0.98	0.99	1.05	1.03
C100×50×6×9			1.01	0.99	1.00	1.06	1.00
		MEAN	1.08	1.05	1.06	1.06	1.04
		COV	0.08	0.06	0.06	0.08	0.06

167

168

169

170



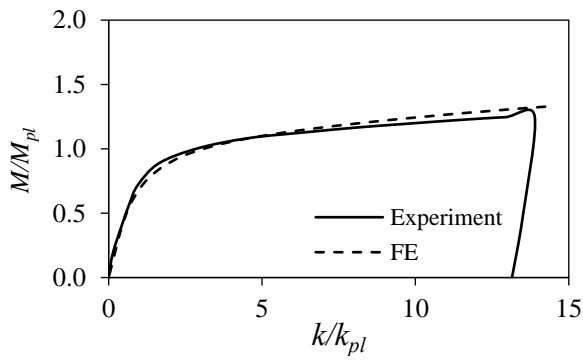
a) B16 [13]

b) C100x50x6x9 – 3-point [14]

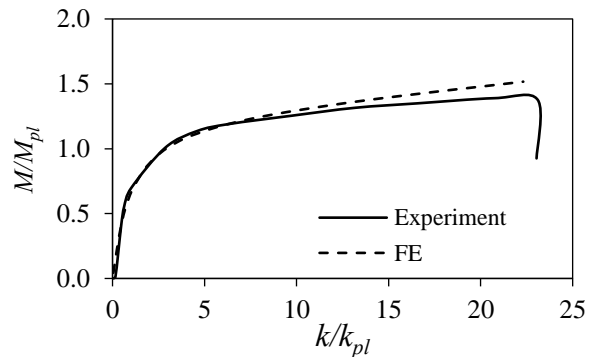
171

Figure 4: Comparison between typical experimental and FE failure modes.

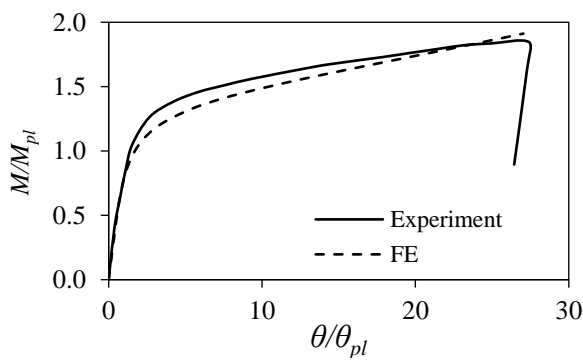
172



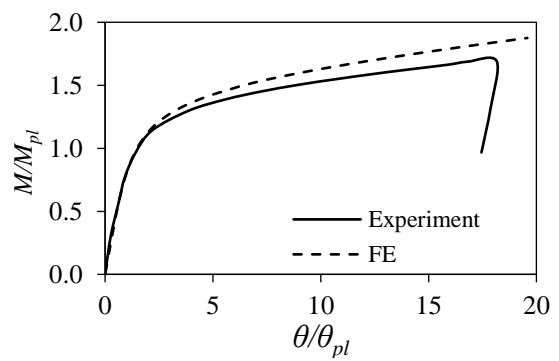
a) B15 (4-point)



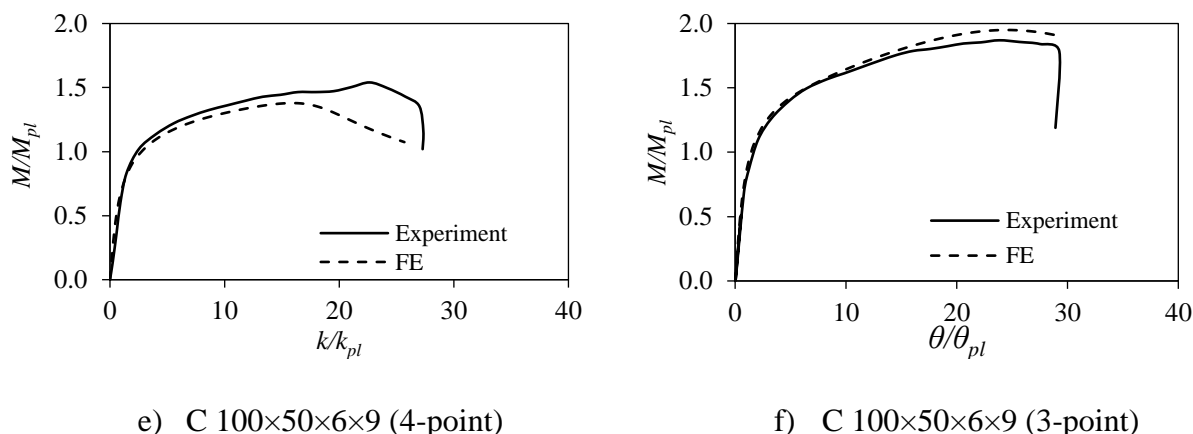
b) B19 (4-point)



c) B8 (3-point)



d) B16 (3-point)



173 Figure 5: Comparison between experimental [13, 14] and numerical response.

174 3 PARAMETRIC STUDY

175 Following the successful validation of the FE model, a parametric study was conducted in
 176 order to investigate the structural performance of stainless steel I- and C-sections subjected to
 177 minor axis bending over a wide range of cross-section dimensions. A total of 180 numerical
 178 results were generated. The list of examined parameters is reported in Table 3. The thickness
 179 of the flange t_f was varied to extend the slenderness range of available results from the very
 180 stocky end of the spectrum to the slender one, i.e., $c_f/(t_f \epsilon)$ in the range of 7.9–39.3. Three cross-
 181 sectional aspect ratios (h/b) were examined. Currently there are experimental results on
 182 outstand elements under stress gradients only for austenitic stainless steels, but no results have
 183 been reported for ferritic or duplex grades. Therefore, in order to expand the performance data
 184 of cross-sections with outstand flanges under stress gradient to other stainless steel grades, the
 185 standardised material properties for austenitic, duplex and ferritic stainless steel grades
 186 proposed in [17] have been adopted herein. The material properties adopted in the parametric
 187 study are shown in Table 4, where n and m are coefficients of the two stage Ramberg-Osgood
 188 material model [19], f_y the 0.2% proof stress and f_u and ϵ_u the ultimate stress and the strain at
 189 ultimate stress, respectively. The resulting stress-strain response is depicted in Figure 6,
 190 showing that the duplex grade has the highest strength, ferritic has the lowest ductility and
 191 austenitic the most pronounced ductility and strain-hardening material properties among the
 192 three grades considered.

193 All FE models had a 1500 mm span and were subjected to 4-point bending with equal loads
 194 applied at third points of the span. The 4-point bending configuration resulted in a uniform
 195 bending moment region over the central 500 mm of the specimen. Note that for both the I- and
 196 the C-sections beam tests [13, 14], it was shown that the 4-point bending configuration led to
 197 lower moment capacity values compared with their 3-point bending counterparts. Hence, it was
 198 considered a conservative and reasonable approach to proceed with 4-point models only in the
 199 parametric study, as it allowed the investigation of the cross-sectional response without the
 200 added complexity of the effect of a moment gradient. The selected imperfection amplitude for
 201 the parametric study was $b/200$, which was applied to the lowest symmetric elastic buckling
 202 mode shape. This imperfection magnitude allowed an accurate replication of the experimental

203 behaviour and was considered a good approximation of real structures imperfections for both
 204 stocky and slender sections. In all analyses, failure was due to local buckling initiated in the
 205 compressed parts of the flange. Typical elastic buckling modes and failure modes are shown in
 206 Figure 7. For all parametric analyses, a moment-curvature curve with a descending branch was
 207 observed, allowing the determination of a distinct ultimate moment value. The numerical
 208 moment resistance of the models was used to evaluate the applicability of design methods to
 209 sections under minor axis bending, as discussed in the following section.

210

211 Table 3: List of parametric studies under minor axis bending.

Total analyses: 180	
2 types of cross-sections	<ul style="list-style-type: none"> • I-sections • C-sections - tip in compression
3 stainless steel materials	<ul style="list-style-type: none"> • Austenitic • Ferritic • Duplex
3 aspect ratios h/b ($h \times b$):	<ul style="list-style-type: none"> • 1.0 (100×100) • 1.5 (100×66.7) • 2.0 (100×50)
10 flange thickness (t_f) Resulting slenderness	<ul style="list-style-type: none"> • 0.5–12 mm • Resulting slenderness: $c/(t_f \epsilon): 7.9\text{--}39.3$ $\bar{\lambda}_{cs}: 0.29\text{--}1.49$ $\bar{\lambda}_p: 0.44\text{--}2.71$

212

213

214 Table 4: Standardised material properties for parametric study [17].

	E (N/mm ²)	f_y (N/mm ²)	f_u (N/mm ²)	n	m	ϵ_u (mm/mm)
Austenitic	200000	280	580	9.10	2.30	0.50
Ferritic	200000	320	480	17.20	2.80	0.16
Duplex	200000	530	770	9.30	3.60	0.30

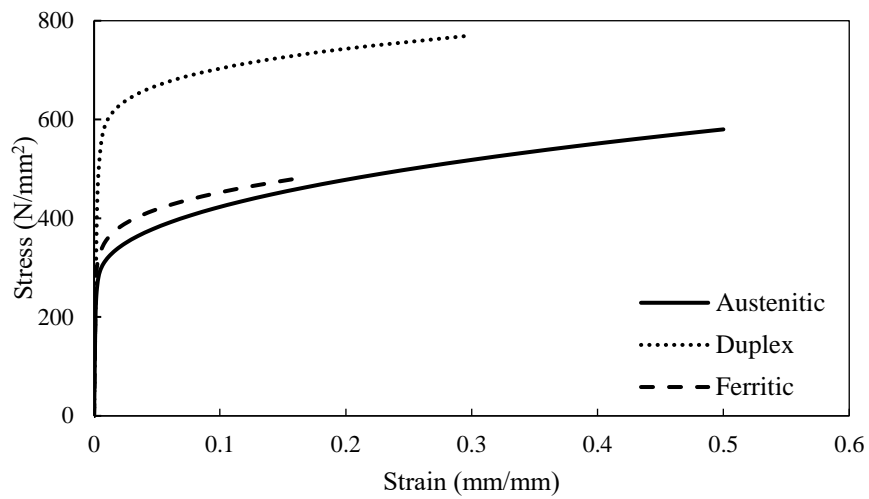
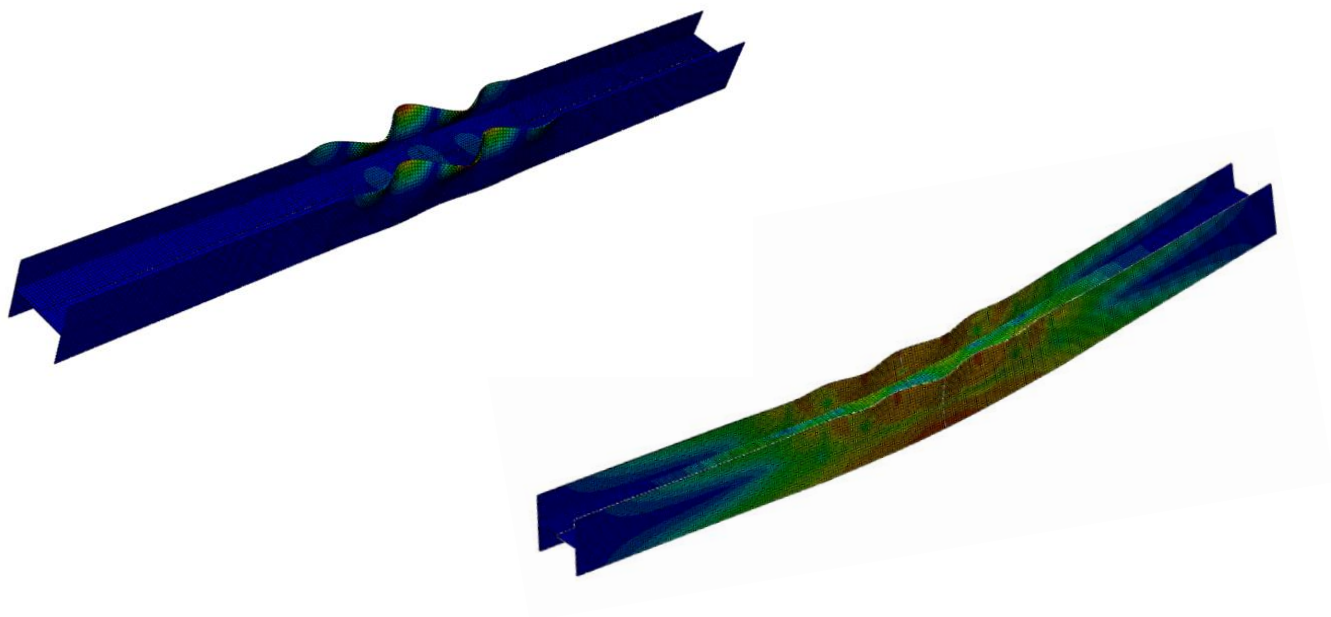
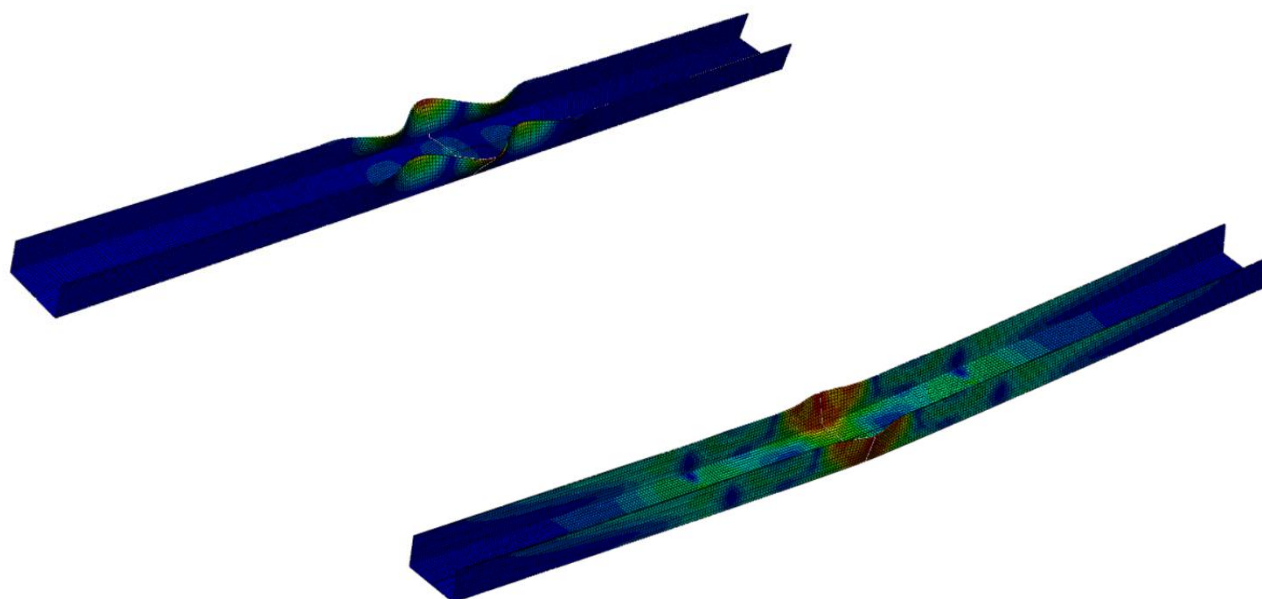


Figure 6: Material properties used for parametric studies [17].

215
216
217



a) I-sections



b) C-sections

218

219 Figure 7: Typical elastic buckling (top) and nonlinear (bottom) failure modes from parametric
220 study.

221 4 ASSESSMENT OF DESIGN PREDICTIONS

222 4.1 EN 1993-1-4 – Slenderness limits for outstand parts

223 The results generated from the parametric study are used herein to assess the applicability of
224 the slenderness limits specified in EN 1993-1-4 [20]. The European design standard for
225 structural stainless steel uses the cross-section classification approach for the treatment of local
226 buckling. The classification of cross-sections is based on four classes which dictate to which
227 extend the resistance and rotation capacity of cross-sections is limited by the effects of local
228 buckling. Class 1 and 2 sections can develop their plastic moment resistance and rotation
229 capacity albeit the extent to which the latter ones rotate is limited due to local buckling. In Class
230 3 sections, the elastic moment resistance can be reached and even exceeded but local buckling
231 prevents the development of their plastic moment resistance; for convenience and to be
232 conservative, the elastic moment resistance is considered as the moment resistance of Class 3
233 sections. Class 4 sections fail by local buckling before the attainment of the cross-section yield
234 resistance.

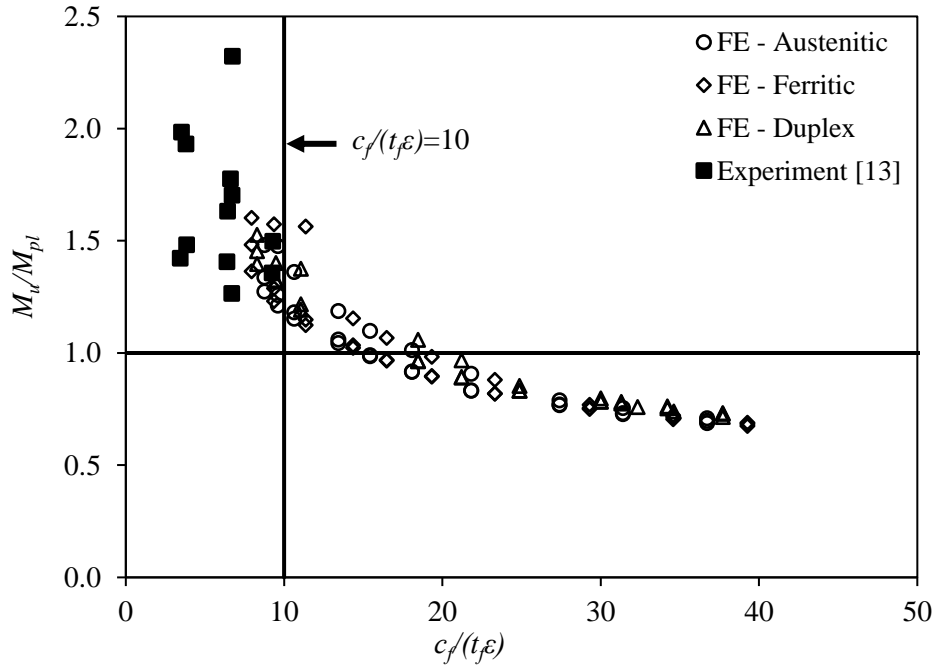
235 To classify a cross-section, the slenderness parameter of each of the cross-sectional parts is
236 compared against slenderness limits and the cross-section is classified as its less favourably
237 classified element. The slenderness limits depend on the stress gradient and the type of cross-
238 section part (i.e., whether internal or outstand). For outstand elements under compressive stress
239 gradient with maximum compression at tip, such as the flanges of an I- section in minor axis
240 bending, the slenderness parameter is $c_f/(t_f \epsilon)$ where c_f is equal to $b/2 - t_w/2$ according to symbols
241 of Figure 1. For outstand elements under bending gradient with the tip in compression, such as

242 the flanges of the examined C-sections, the slenderness parameter for the Class 2 limit is
243 $(\alpha c_f)/(t_f \epsilon)$, where α is the ratio of the width of the compressive portion of the flange to the flat
244 width of the flange, c_f is equal to $b-t_w$ considering symbols shown in Figure 1 and the rest as
245 previously defined. The slenderness parameter for Class 3 limit of the same sections is
246 $c_f/(t_f \epsilon k_\sigma^{0.5})$ where k_σ is the plate buckling coefficient defined in [21] and equal to $0.57-$
247 $0.21\psi+0.07\psi^2$ where ψ is the end tensile to compressive stress ratio of the flat part of the flange.
248 It is noted that numerous experimental results for internal and outstand elements in compression
249 and internal elements in bending were available, whilst no test data on outstand elements in
250 bending were available when the currently codified slenderness limits [20] were proposed [1].
251 As presented in [1], the Class 3 and Class 2 limits for outstand elements in compression were
252 obtained following a statistical analysis using all available test data at the time, whereas in
253 absence of test data for elements under stress gradient, the respective slenderness limits were
254 inferred from the relevant limits for outstand element in compression using buckling factors to
255 account for the difference in the applied stresses and no statistical validation has been
256 performed.

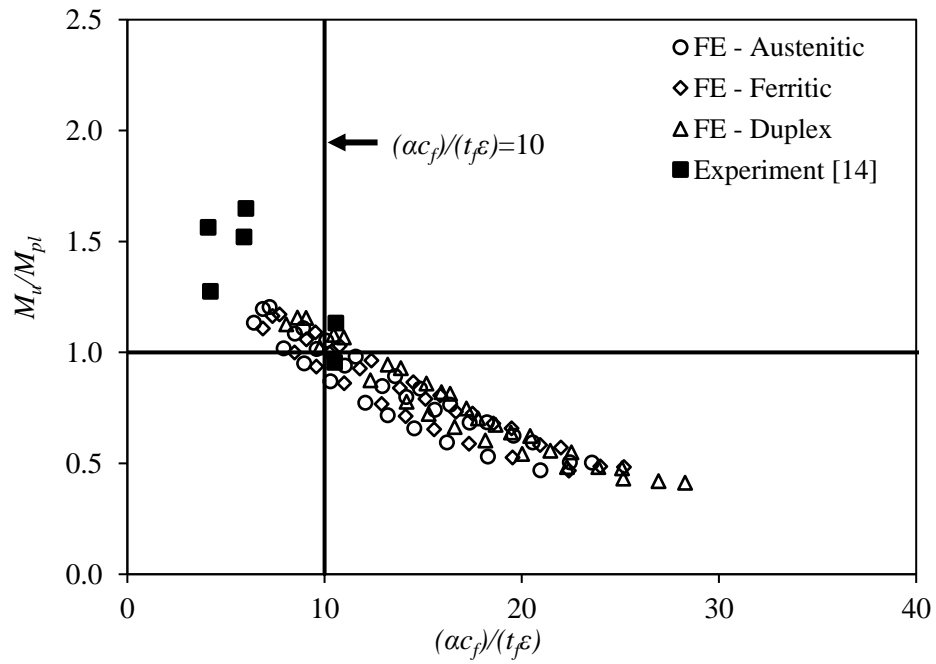
257 The numerical results generated herein have been used to assess the Class 2 slenderness
258 limits for outstand flanges when the tip is subject to compression, as shown in Figure 8. The
259 figure shows the moment resistance obtained from the numerical models M_u normalised by the
260 plastic moment capacity M_{pl} and plotted against the relevant slenderness parameter. It can be
261 observed that the FE results in the stocky range present lower normalised capacities compared
262 to the test values. Given that the stocky sections are mainly affected by material response, whilst
263 the effect of imperfections is minimal, the underestimated capacities could be related to
264 underestimating slightly the true material response. According to [14], the experimentally
265 determined stress values were static values and obtained by pausing the tensile tests for 2 min
266 when approaching the 0.2% and 1% proof stresses and the ultimate stress, whereas no such
267 pause was applied in the bending tests, the material of which did not experience relaxation.
268 Overall the results in Figure 8 show that the bending resistance decreases with increasing cross-
269 section slenderness, whereas the current slenderness limit appears generally safe without being
270 overly conservative.

271 The assessment of the Class 3 slenderness limit for outstand elements under stress gradient
272 is presented in Figure 9, where the moment resistance M_u normalised by the elastic moment
273 capacity M_{el} is plotted against the slenderness parameter. For both I- and C-sections, the current
274 EN 1993-1-4 Class 3 slenderness limits [20] are overly conservative and could be relaxed, as
275 cross-sections with flange slenderness limits as high as 40 and 30 for I- and C-sections,
276 respectively, are still able to develop their elastic moment resistance. This observation is in line
277 with recent research studies on high strength steel channel sections under minor axis bending
278 with tip in compression, where it was concluded that Class 3 Eurocode limit is excessively
279 conservative [22-24].

280



a) I-sections

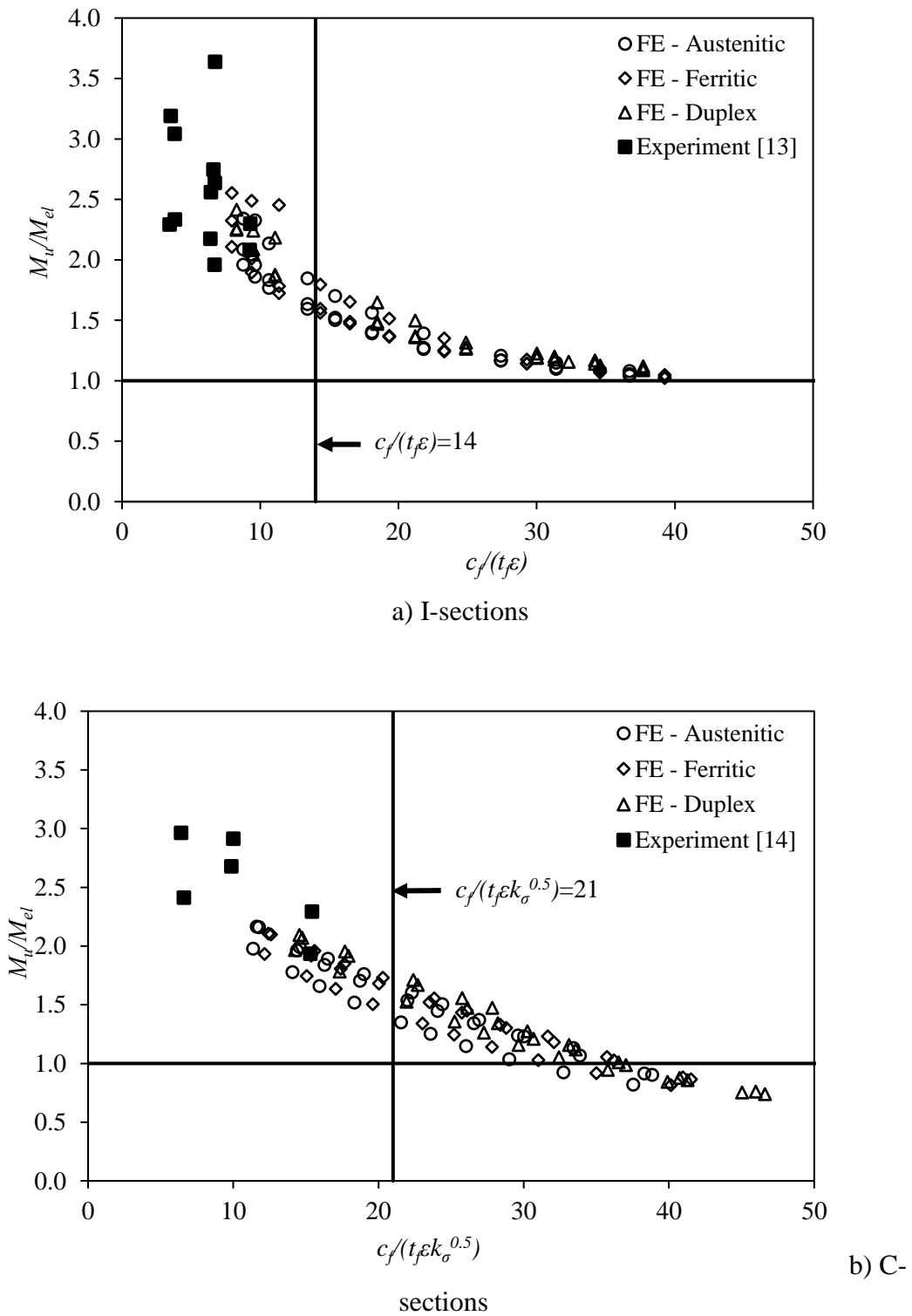


b) C-sections

281

Figure 8: Assessment of Class 2 slenderness limits for outstand elements.

282



283 Figure 9: Assessment of Class 3 slenderness limit for outstand elements.

284 **4.2 EN 1993-1-4 – Strength predictions**

285 In this section, the accuracy of the Eurocode predictions is assessed based on the ultimate
 286 bending capacities of I- and C-sections under minor axis bending. The cross-section flexural

287 strengths according to EN 1993-1-4 [18] (M_{pred}) are equal to plastic ($W_{pl}f_y$), elastic ($W_{el}f_y$) and
288 effective ($W_{eff}f_y$) moment capacities for Class 1 or 2, for Class 3 and Class 4 sections,
289 respectively. W_{pl} and W_{el} are the plastic and elastic section modulus on the relevant bending
290 axis (minor axis herein) and W_{eff} is the effective section modulus determined based on the
291 reduced cross-sectional area excluding the areas that are ineffective due to local bulking. In
292 order to determine the effective area of Class 4 cross-sections, the effective width (b_{eff}) of
293 slender constituent elements under compression of width b is calculated according to Eq. (3)

$$b_{eff} = b\rho \quad (3)$$

294 Where ρ is a local buckling reduction factor provided by Eq. (4) for outstand compression
295 elements

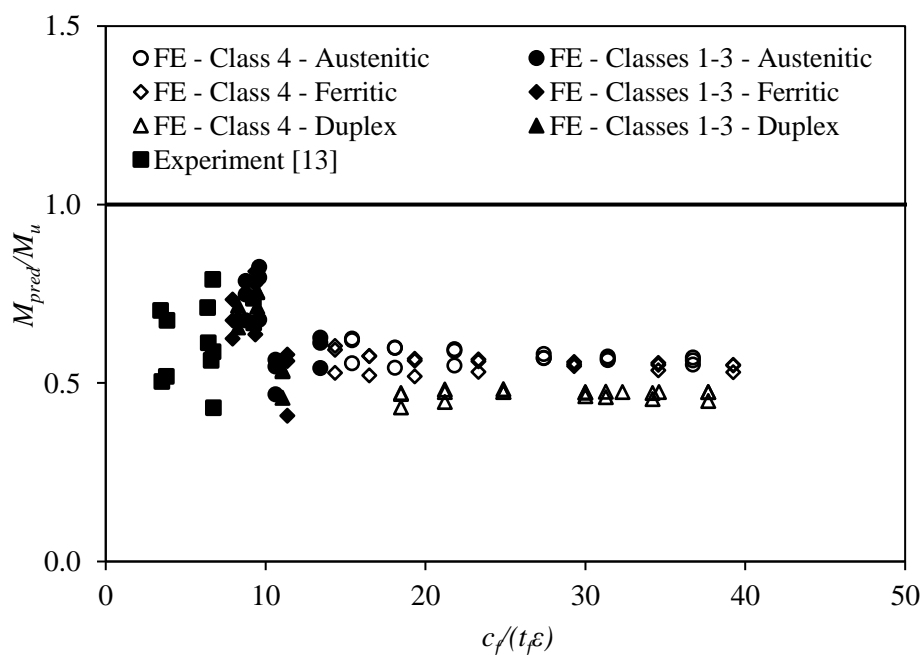
$$\rho = \left(\frac{1}{\bar{\lambda}_p} - \frac{0.188}{\bar{\lambda}_p^2} \right) \leq 1 \quad (4)$$

296 $\bar{\lambda}_p$ is the plate slenderness from Eq. (5)

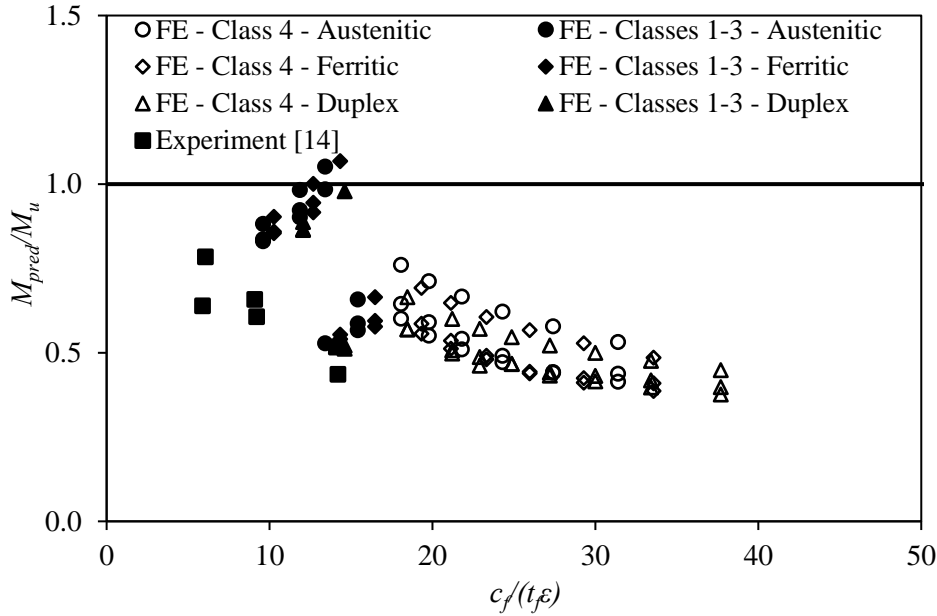
$$\bar{\lambda}_p = \frac{c_f / t_f}{28.4\varepsilon\sqrt{k_\sigma}} \quad (5)$$

297 and k_σ is the plate buckling coefficient defined in [21] as a function of the stress ratio ψ .

298 Figure 10 presents the predicted-to-ultimate (M_{pred}/M_u) moment ratio plotted against the
299 slenderness parameter $c_f/(t_f\varepsilon)$. The figure shows separately the FE slender (Class 4) and stocky
300 (Class 1-3) sections. Clearly, for both I-sections and C-sections Eurocode overly underestimates
301 the flexural capacity. This is quite pronounced for slender cross-sections, revealing the
302 conservatism of the effective width approach. The overly conservative Class 3 limit also affects
303 the quality of the design predictions. The predictions in the stocky range appear quite scattered
304 and underestimated owing to the lack of consideration of the material strain-hardening, as will
305 be further discussed in the following section.



a) I-sections



b) C-Sections

306 Figure 10: Assessment of EN 1993-1-4 design predictions.

307 4.3 Continuous Strength Method

308 The apparent disparity between the Eurocode design predictions and the moment resistances
309 for stocky sections that was shown in Figure 10 has been extensively documented in past studies
310 [1-16] and is attributed to the material strain-hardening which allows non-slender sections to
311 reach stresses higher than their nominal yield strength. The Continuous Strength Method (CSM)
312 was therefore developed as a rational design approach that allows exploitation of the material
313 strain-hardening in the design predictions for stocky cross-sections [25]. The method has been
314 recently extended to cover slender cross-sections [26, 27]. The CSM assumes an elastic linear
315 hardening material model and the strain at which failure due to local buckling occurs (ε_{csm}) is
316 determined as a function of the cross-sectional slenderness $\bar{\lambda}_{cs}$ and the yield strain ε_y , according
317 to Eq. (6)

$$\varepsilon_{csm} = \frac{0.25}{\bar{\lambda}_{cs}^{3.6}} \varepsilon_y \leq \min \left(15, \frac{C_1 \varepsilon_u}{\varepsilon_y} \right) \text{ for } \bar{\lambda}_{cs} \leq 0.68 \quad (6)$$

$$\varepsilon_{csm} = \left(1 - \frac{0.222}{\bar{\lambda}_{cs}^{1.05}} \right) \frac{1}{\bar{\lambda}_{cs}^{1.05}} \varepsilon_y \text{ for } \bar{\lambda}_{cs} > 0.68$$

318 Where the coefficient C_1 is equal to 0.1 for austenitic and duplex stainless steels and 0.4 for
319 ferritic stainless steels [26].

320 The cross-sectional slenderness $\bar{\lambda}_{cs}$ is provided by Eq. (7)

$$\bar{\lambda}_{cs} = \sqrt{\frac{f_y}{f_{cr}}} \quad (7)$$

321 Where f_{cr} is the elastic critical buckling stress. In order to evaluate the elastic critical buckling
 322 stress accounting for element interaction, analytical expressions have been previously proposed
 323 [28, 29]. In both cases [28, 29], the authors performed an extensive number of finite strip
 324 analysis in CUFSM software, calibrated the results and derived formulae for the elastic critical
 325 buckling stress of various cross-sectional shapes under different loading conditions. Herein, the
 326 equations proposed in [28] are used for the determination of f_{cr} . In particular, f_{cr} is calculated
 327 from Eq. (8) considering the symbols defined in Figure 1 and the Poisson's ratio ν equal to 0.3
 328 for stainless steels.

$$f_{cr} = k_w \frac{\pi^2 E}{12(1-\nu^2)} \left(\frac{t_w}{h-t_f} \right)^2 \quad (8)$$

329 where k_w the local plate buckling coefficient, which accounts for the boundary and loading
 330 conditions, evaluated from Eqs. (9) and (10) [28] for I-sections under minor axis bending and
 331 for C-sections under minor axis bending and tip in compression, respectively.

$$k_w = \frac{1}{0.008 + \frac{1.5}{\left(\left(\frac{h-t_f}{t_w} \right) \left(\frac{2t_f}{b} \right) \right)^{2.5}}} \quad (9)$$

$$k_w = \frac{\left(\left(\frac{h-t_f}{t_w} \right) \left(\frac{t_f}{b} \right) \right)^2}{0.8} \quad (10)$$

332 According to the CSM, the flexural strength in minor axis bending can then be evaluated by
 333 Eq. (11)

$$M_{pred} = \frac{\varepsilon_{csm}}{\varepsilon_y} W_{el} f_y \quad \text{for } \frac{\varepsilon_{csm}}{\varepsilon_y} < 1$$

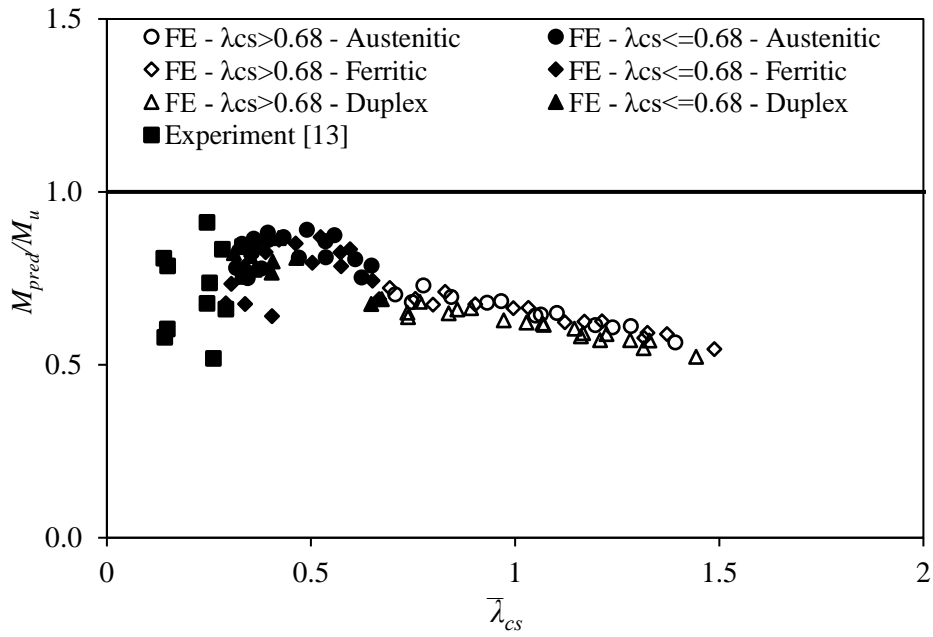
$$M_{pred} = W_{pl} f_y \left[1 + \frac{E_{sh}}{E} \frac{W_{el}}{W_{pl}} \left(\frac{\varepsilon_{csm}}{\varepsilon_y} - 1 \right) - \left(1 - \frac{W_{el}}{W_{pl}} \right) / \left(\frac{\varepsilon_{csm}}{\varepsilon_y} \right)^\alpha \right] \quad \text{for } \frac{\varepsilon_{csm}}{\varepsilon_y} \geq 1 \quad (11)$$

334 where α is equal to 1.2 for I-sections in minor axis bending and equal to 1.5 for C-sections
 335 under minor axis bending and $h/b \leq 2$ [27] and E_{sh} is the strain-hardening modulus of the CSM
 336 linear hardening material model from Eq. (12)

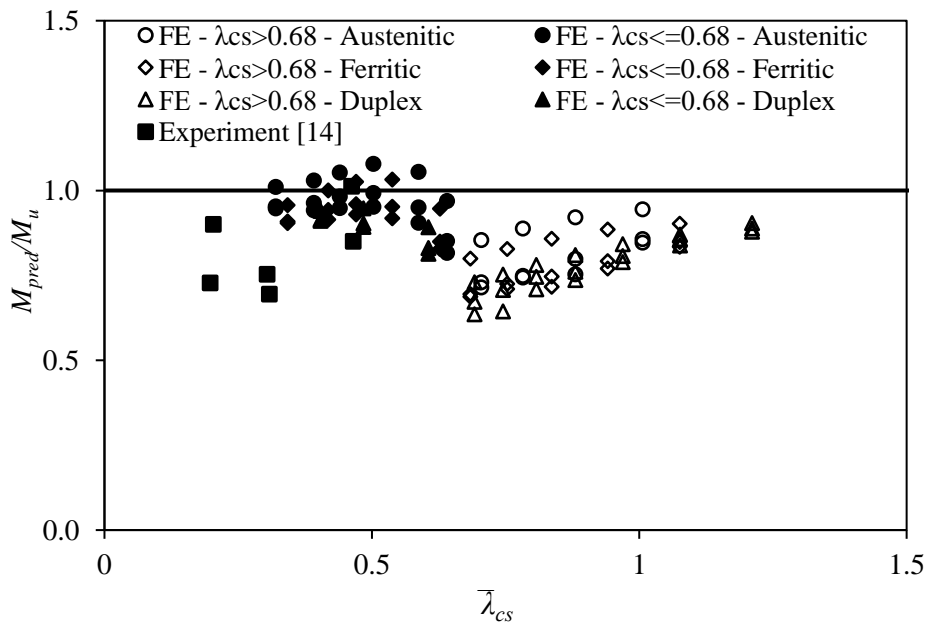
$$E_{sh} = \frac{f_u - f_y}{C_2 \varepsilon_u - \varepsilon_y} \quad (12)$$

337 where the coefficient C_2 is equal to 0.16 for austenitic and duplex stainless steels and 0.45 for
 338 ferritic stainless steels [26]. The remaining material properties are calculated according to Table
 339 4 for this study. The predicted-to-ultimate strength ratios are shown in Figure 11. Compared to
 340 the EN 1993-1-4, it can be observed that the CSM offers significantly improved strength
 341 predictions in terms of accuracy and consistency for stocky cross-sections. However, it can be
 342 observed that the CSM predictions for slender sections are overly conservative, particularly for
 343 I-sections.

344



a) I-sections



b) C-sections

345

Figure 11: Assessment of the Continuous Strength Method.

346

4.4 Direct Strength Method

347

The direct strength method (DSM) was developed by [30, 31] for cold-formed members in order to overcome the complicated calculation process involved in the effective width approach when applied to cross-sections of complex geometries. It was extended to cover stainless steel cross-sections by [32-34]. The DSM relates the resistance of sections to the cross-sectional slenderness $\bar{\lambda}_{cs}$, thus allowing the beneficial effect of the element interaction of a cross-section to be considered, contrary to the element-by-element approach employed by the traditional effective width method. Even though DSM was originally applied only for slender sections, Eq.

353

354 (13) [34] was suggested for stainless steels in order to evaluate the moment resistance of cross-
355 sections across the full slenderness range.

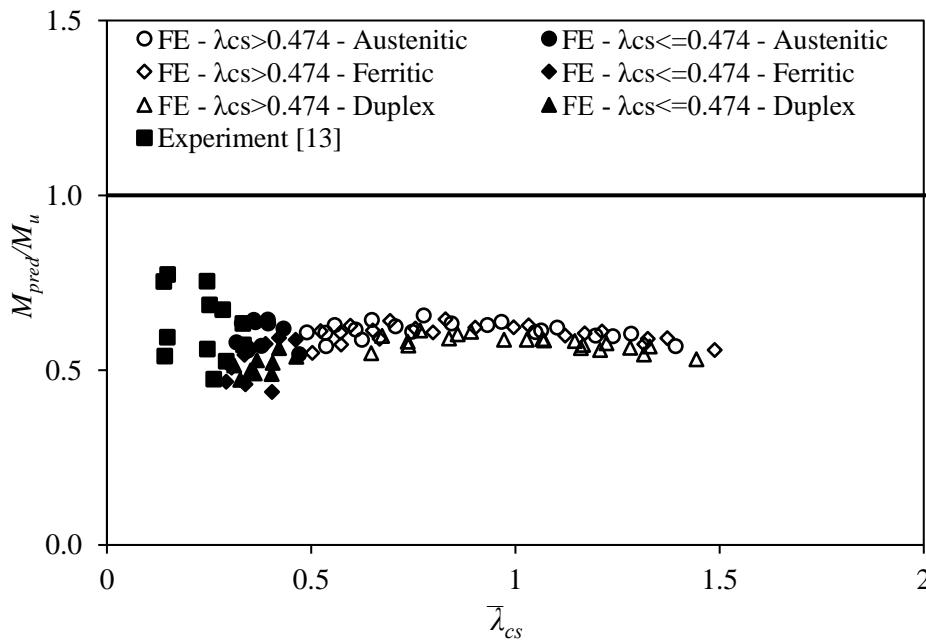
$$M_{pred} = \left(\frac{0.95}{\bar{\lambda}_{cs}^{0.8}} - \frac{0.22}{\bar{\lambda}_{cs}^{1.6}} \right) (W_{el} f_y) \quad \text{for } \bar{\lambda}_{cs} > 0.474$$

$$M_{pred} = [1 + (1 - 2.11 \bar{\lambda}_{cs}) \left(\frac{f_u}{f_y} - 1 \right)] (W_{el} f_y) \quad \text{for } \bar{\lambda}_{cs} \leq 0.474$$
(13)

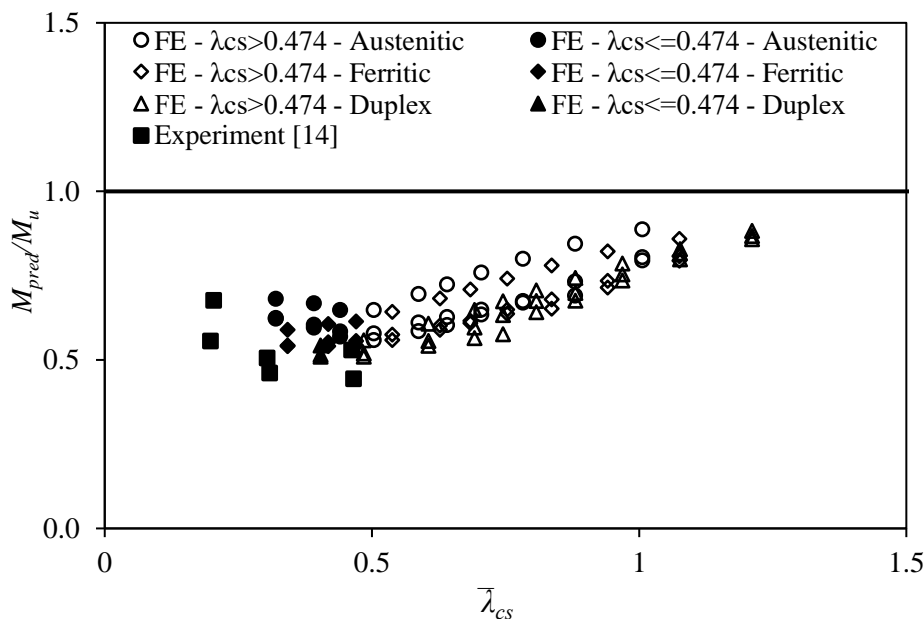
356 where $\bar{\lambda}_{cs}$ is determined from Eq. (7).

357

358 The numerical results have been used to assess the applicability of the DSM to both stocky and
359 slender stainless steel cross-sections. In Figure 12, the predicted moment resistances are
360 normalised by the numerical ultimate strengths and plotted against the cross-sectional
361 slenderness. For I-sections, the FE results suggest that the design estimations are consistently
362 conservative, significantly underestimating the flexural strength throughout the slenderness
363 range considered. On the other hand, more scattered predictions with increased accuracy for
364 higher cross-section slenderness values, are observed for C-sections. The observed discrepancy
365 can be partly attributed to the lack of consideration of the neutral axis shift which takes place
366 with the onset of local buckling in slender sections. A more significant source of error is
367 believed to be the actual stress distribution that cross-sections with outstand elements
368 experience at failure, which deviates from the assumed linear one, as discussed in the following
369 section. The incorrect consideration of the stress distribution has a significant effect on the
370 design predictions of I-sections where the contribution to moment resistance of both the tensile
371 and the compressive flanges is incorrectly estimated. The latter could be related with the fact
372 design predictions for the methods presented in Sections 4.3 and 4.4 are generally more
373 conservative for I-sections compared to those for the C-sections.



a) I-sections



b) C-sections

374 Figure 12: Assessment of the Direct Strength Method for stainless steels.

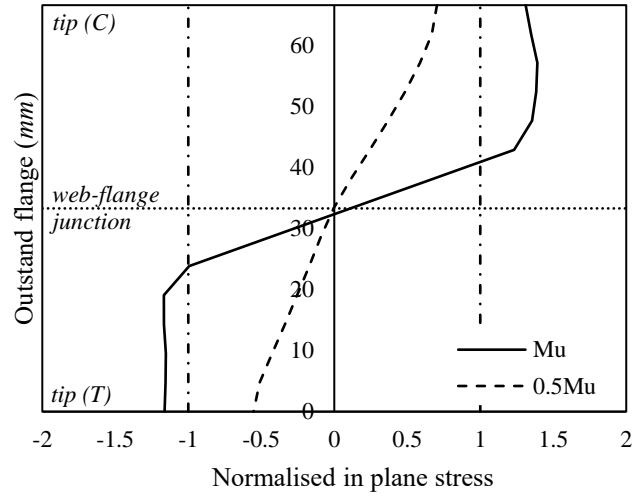
375

376 4.5 Plastic Effective Width Method

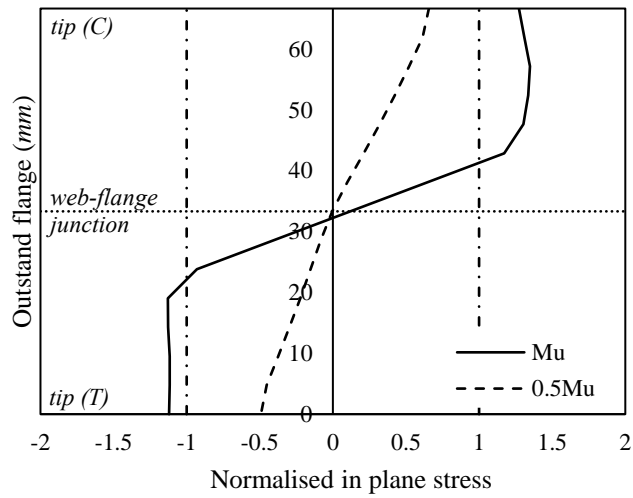
377 Research on the structural behaviour of slender steel I-sections under minor axis bending
 378 [35] has shown that the current design model assumed for slender I-sections is fundamentally
 379 incorrect. Despite slender outstands in bending not attaining their elastic moment resistance, it
 380 has been shown that the stress distribution is not linear, as commonly assumed, but contains
 381 regions subjected to nonlinear stresses. In order to assess the applicability of these observations
 382 to stainless steel sections, the generated FE are utilised. Figures 13 and 14 depict the in-plane
 383 longitudinal stresses distribution over the flange at mid-span of I- and C-sections, respectively.
 384 Since slender outstand elements experience local buckling at failure, the stress values extracted
 385 were obtained from the integration points at mid-thickness of the sections, thus excluding any
 386 bending strength components. The figures show the results for the most slender examined cross-
 387 sections with $h/b=1.5$, while similar is the response for all other slender sections. Moreover, the
 388 results are presented normalised with the proof strength of each stainless steel type. The web-
 389 flange junction and the tip (C for compression and T for tension) is included in the figures. The
 390 stress patterns prior to failure ($0.5M_u$) and at failure (M_u) are also shown.

391 For I-sections under minor axis bending, nonlinear stresses can be seen on both the tension
 392 and on the compression side. Even for very slender sections, the initially linear elastic stress
 393 distribution becomes highly nonlinear with well-defined stress blocks reminiscent of the plastic
 394 stress blocks corresponding to the attainment of the plastic moment resistance, albeit not
 395 extending throughout the section height. Furthermore, significant strain-hardening in both
 396 tension and compression is observed for all 3 material grades considered. These observations
 397 are in agreement with Figure 9(a), where all sections comfortably exceeded their elastic moment

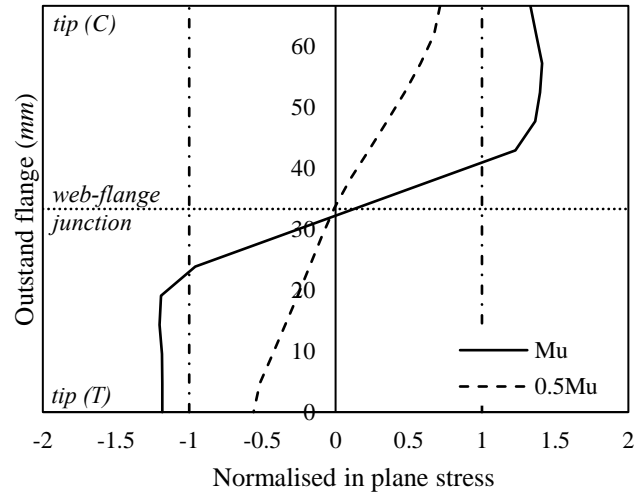
398 resistance regardless even when the slenderness of the flange was 3 times the limiting value for
 399 Class 3 sections. It can also be noticed a decrease in stress in the compressed tips; this reduction
 400 in the longitudinal carrying capacity could be related with the development of high transverse
 401 stresses due to local buckling in addition to the longitudinal ones.
 402



a) Austenitic ($100 \times 66.67 \times 1$ - $h/b=1.5$, $c_f/(t_f \epsilon)=36.7$, $\lambda_{cs}=1.28$)



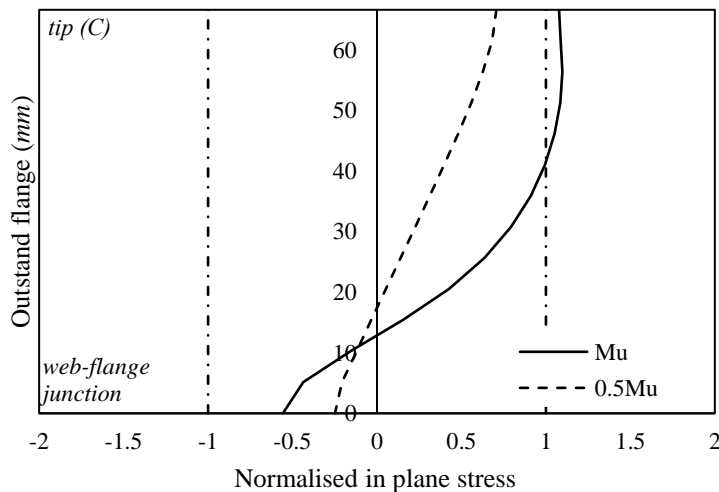
b) Ferritic ($100 \times 66.67 \times 1$ - $h/b=1.5$, $c_f/(t_f \epsilon)=39.2$, $\lambda_{cs}=1.37$)



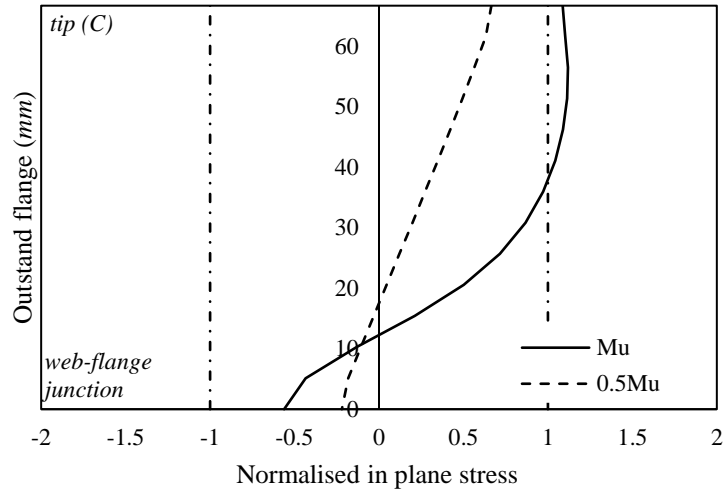
c) Duplex ($100 \times 66.67 \times 1.33 - h/b=1.5, c_f/(t_f \epsilon)=37.7, \lambda_{cs}=1.33$)

403 Figure 13: Development of longitudinal stresses over the flange at mid-span of typical
 404 slender I-sections.

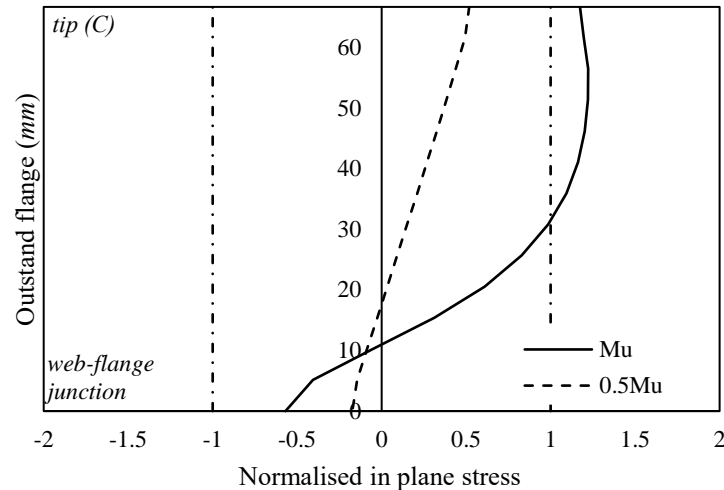
405 In C-sections in bending, as clearly shown in Figure 14, stresses higher than the yield stress
 406 develop even when the section fails prior to the attainment of its elastic moment resistance.
 407 Furthermore, the shift of the neutral axis towards the web for slender sections at failure is also
 408 clearly observed. Hence, assuming a linear stress distribution over an effective section with a
 409 stress limit of f_y is not in accordance with the observed response and leads to overly conservative
 410 and fundamentally incorrect strength predictions. Therefore, alternative approaches accounting
 411 for the plastic reserve of cross-sections with locally bucked outstands have been developed for
 412 carbon steel. These methods known as plastic effective with methods are based on the
 413 determination of effective widths of the section considering an inelastic stress distribution.



a) Austenitic ($100 \times 66.7 \times 2.33 - h/b=1.5, c_f/(t_f \epsilon)=31.4, \lambda_{cs}=1.01$)



b) Ferritic ($100 \times 66.7 \times 2.33 - h/b=1.5, c_f/(t_f \epsilon)=33.6, \bar{\lambda}_{cs}=1.08$)



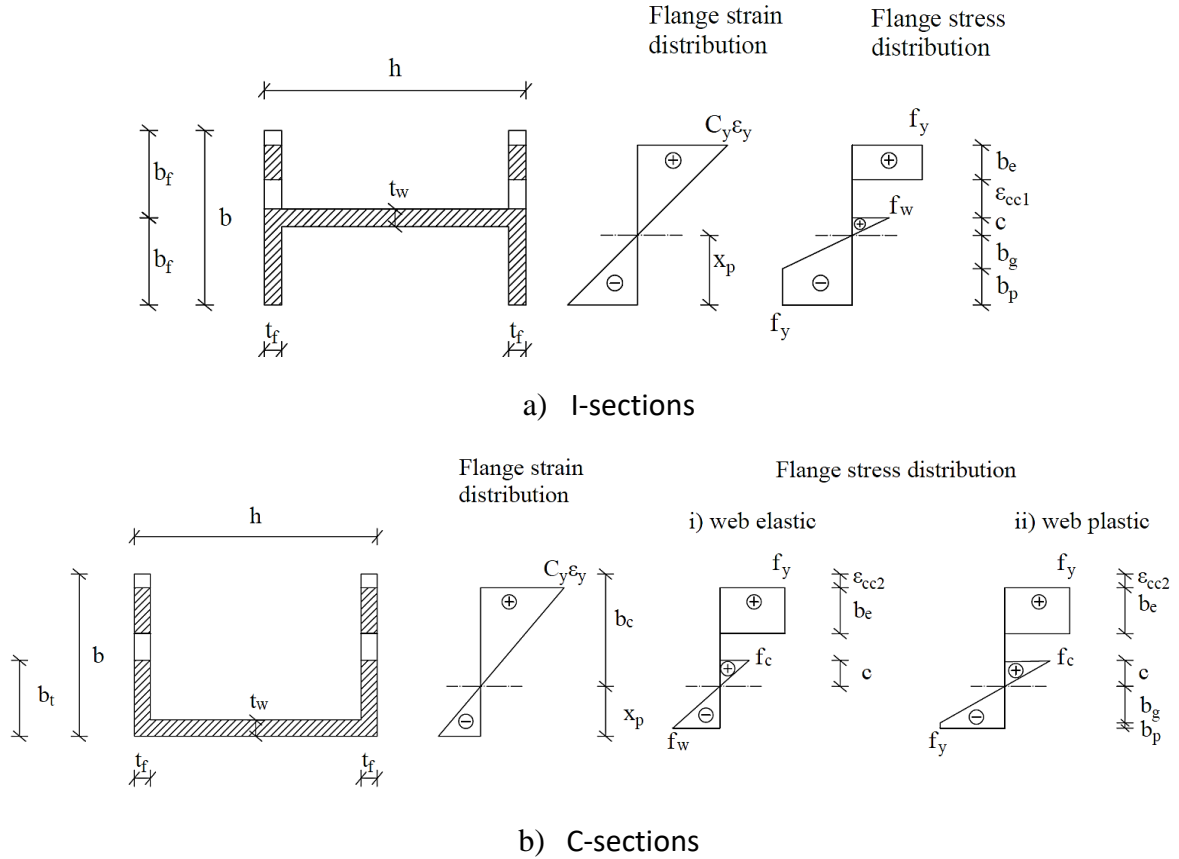
c) Duplex ($100 \times 66.7 \times 2.67 - h/b=1.5, c_f/(t_f \epsilon)=37.7, \bar{\lambda}_{cs}=1.21$)

414 Figure 14: Development of longitudinal stresses over the flange at mid-span of typical
 415 slender C-sections.
 416

417 The method considered herein was proposed by [35] for slender hot-rolled and cold-formed I-
 418 sections with flanges subject to stress gradients. This method considers a bilinear elastic
 419 perfectly plastic stress distribution. As stainless steels exhibit significant strain-hardening such
 420 a model is expected to underestimate the stresses corresponding to the plastic effective width,
 421 particularly for the parts of the section the farthest away from the neutral axis. This is clearly
 422 observed in Figures 13 and 14, where the stress values obtained from the FE analysis close to
 423 the extreme compression fibre were well in excess of the nominal yield stress. However, in the
 424 interest of not overcomplicating the proposed design method and given that in current design
 425 procedures for Class 4 sections only stresses lower than the nominal yield stress are allowed, it
 426 was decided not to explicitly consider the effect of strain-hardening in the design model for
 427 Class 4 sections proposed herein.

428 The plastic width effective method considers the post-buckling reserve capacity of slender
 429 sections according to the stress and strain distributions shown in Figure 15. The method

430 suggests that when a slender I- or C-section is subjected to minor axis bending, the strain of the
431 compressive outstand tip at failure exceeds the yield strain (ε_y) by a coefficient C_y . For I-
432 sections, the locally buckled compressive flange behaves plastically for a width equal to b_e and
433 at a distance e_{cc1} from the web. The procedure suggested by Bambach et al. [35] for I-sections
434 is given in Equations (14)-(25). The coefficients C_y , b_e and e_{cc1} are initially evaluated by Eqs.
435 (14) - (16). Following, the neutral axis for the new effective section (x_p) can be calculated from
436 Eq. (18) and the moment resistance (M_{pred}) on the basis of the stress blocks of the effective
437 section can be calculated by Eqs. (19)-(25). The symbols of these equations are in line with
438 Figure 15(a).



439

440 Figure 15: Plastic effective width method – strain and stress distribution of the flanges.

441

$$C_y = 3 \quad (14)$$

$$b_e = b_f 0.4 \bar{\lambda}_{cs}^{-0.75} \quad (15)$$

$$e_{cc1} = 0.45 b_f \quad (16)$$

$$b_f = 0.5 b \quad (17)$$

$$x_p = \frac{2b_e t_f [(2b_f - b_e / 2) - (b_f - b_e - e_{cc1})] + 2b_f t_f b_f / 2 + (h - 2t_f) t_w b_f}{2b_e t_f + 2b_f t_f + (h - 2t_f) t_w} \quad (18)$$

$$b_p = x_p - b_g \quad (19)$$

$$b_g = \varepsilon_y / K \text{ where} \quad (20)$$

$$\varepsilon_y = f_y / E \quad (21)$$

$$K = \frac{C_y \varepsilon_y}{b_f - x_p + e_{cc1} + b_e} \quad (22)$$

$$c = b_f - b_g - b_p \quad (23)$$

$$f_w = (cK)E \quad (24)$$

$$M_{pred} = 2b_e t_f f_y (e_{cc1} + \frac{b_e}{2} + c) + 2b_p t_f f_y (x_p - \frac{b_p}{2}) + \frac{2}{3} b_g^2 f_y t_f + \frac{2}{3} c^2 f_w t_f + (h - 2t_f) t_w f_w c \quad (25)$$

442 Adopting a similar concept for C-sections, the procedure suggested by Bambach et al. [35] for
 443 C-sections is given in Equations (26)-(38). The outstand flange is subjected to $C_y \varepsilon_y$ strain at
 444 failure according to Eq. (26), whereas the plastic effective width b_e can be evaluated by Eq.
 445 (27) and is at a distance e_{cc2} (according to Eq. (28)) from the tip. Upon calculation of the neutral
 446 axis, the M_{pred} can be calculated by the sum of the stress blocks of the effective section from
 447 Eqs. (29)-(38), where all symbols are defined in Figure 15(b). Note that depending on the
 448 geometrical properties and thus the flange's strain distribution, the web can either be under
 449 elastic stress state (Figure 15(b) i) and Eq. 38(a)) or in the plastic regime (Figure 15(b) ii) and
 450 Eq. 38(b)).

$$C_y = 3.67 - 1.98 b_f / t_f \sqrt{\frac{f_y}{E}} \text{ and } 1 \leq C_y \leq 3 \quad (26)$$

$$b_e = 0.4(1 + \psi) \bar{\lambda}_{cs}^{-0.75} b \leq b_c \quad (27)$$

$$e_{cc2} = 0.55(1 + \psi) b - b_e \quad (28)$$

$$x_p = \frac{2b_e t_f (b - b_e / 2 - e_{cc2}) + 2b_t t_f b_t / 2 + (h - 2t_f) t_w t_w / 2}{2b_e t_f + 2b_t t_f + (h - 2t_f) t_w} \quad (29)$$

$$b_t = \frac{b^2 t_f + (h - 2t_f) t_w^2 / 2}{2b t_f + (h - 2t_f) t_w} \quad (30)$$

$$b_g = \varepsilon_y / K \text{ where} \quad (31)$$

$$K = \frac{C_y \varepsilon_y}{b - x_p - e_{cc2}} \quad (32)$$

$$\varepsilon_y = f_y / E \quad (33)$$

$$b_c = b - x_p \quad (34)$$

$$b t_w = x_p - 0.5 t_w - b_g \text{ if } b_g < x_p - 0.5 t_w \quad (35)$$

$$f_w = (x_p - 0.5 t_w) K E \quad (36)$$

$$f_c = (cK)E \quad (37)$$

$$M_{pred} = 2b_e t_f f_y (b - e_{cc2} - \frac{b_e}{2} - x_p) + \frac{2}{3} f_c t_f c^2 + \frac{2}{3} f_w t_f (x_p - 0.5t_w)^2 + (h - 2t_f) t_w f_w (x_p - 0.5t_w) \quad (38a)$$

$$M_{pred} = 2b_e t_f f_y (b - e_{cc2} - \frac{b_e}{2} - x_p) + \frac{2}{3} f_c t_f c^2 + \frac{2}{3} f_y t_f b_g^2 + 2b_p t_f f_y (b_g + b_p / 2) + (h - 2t_f) t_w f_y (x_p - 0.5t_w) \quad (38b)$$

451

452 It is noteworthy that even though the investigation in [35] was mainly focussed on I-sections,
453 the authors have also recommended equations for C-sections, suggesting the calculation of the

454 strain coefficient C_y as a function of $b_f / t_f \sqrt{\frac{f_y}{E}}$ (Eq. (26)). However, utilising the stress and

455 strain distributions of the slender C-sections of this study, new equations with a better

456 agreement to the numerical results are recommended for stainless steel C-sections. As shown

457 in Figure 15(b), C_y is the strain coefficient at distance e_{cc2} from the compressive tip. Upon

458 exporting the FE in-plane longitudinal strain distributions of all slender profiles, $C_{y, FE}$ was

459 calculated as the ratio of the strain at ultimate load at the reference location ($\varepsilon_{u, ecc2}$) over the

460 yield strain (ε_y). As can be seen in Figure 16(a), the $C_{y, FE}$ values were found to linearly correlate

461 with $\bar{\lambda}_{cs}^{-0.75} (1 + \psi)$, which is one of the functions already used within the method (see Eq. (27)).

462 The C_y predicted values ($C_{y, pred}$) from Eq. (26) [35] and from the proposed Eq. (39) are also

463 assessed in Figure 16 (b) showing improved estimation for the latter. Subsequently, Eq. (27)

464 has been recalibrated to Eq. (40) on the basis of $M_{u, pred} / M_{u, FE}$ values in order to improve design

465 accuracy and consistency (i.e., $M_{u, pred} / M_{u, FE}$ ratios closer to unity and with smaller COVs).

466 Hence, Eqs. (39)-(40) are proposed for C-sections instead of the previously suggested Eqs. (26)-

467 (27).

468 Moreover, the equations of this method (i.e., Eqs. (14)-(25) for I-sections and Eqs. (28)-(40)

469 for C-sections) were assessed by comparing the FE stress profiles with those found by the

470 design equations. Examples of this comparison is presented in in Figure 17, where it can be

471 seen a very good agreement between numerical and theoretical predictions.

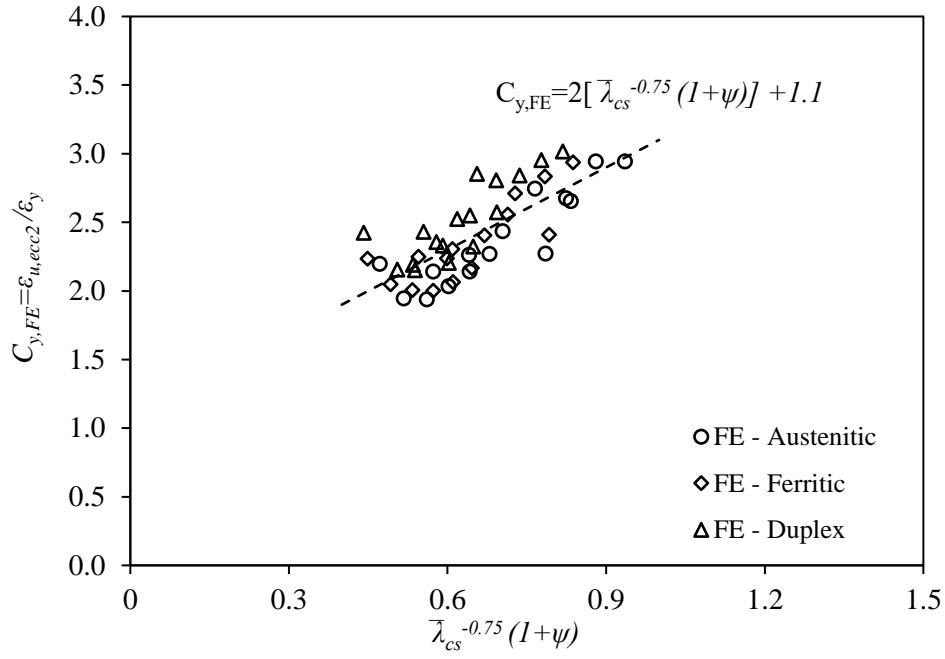
472

$$C_y = 2(1 + \psi) \bar{\lambda}_{cs}^{-0.75} + 1.1 \leq 3 \quad (39)$$

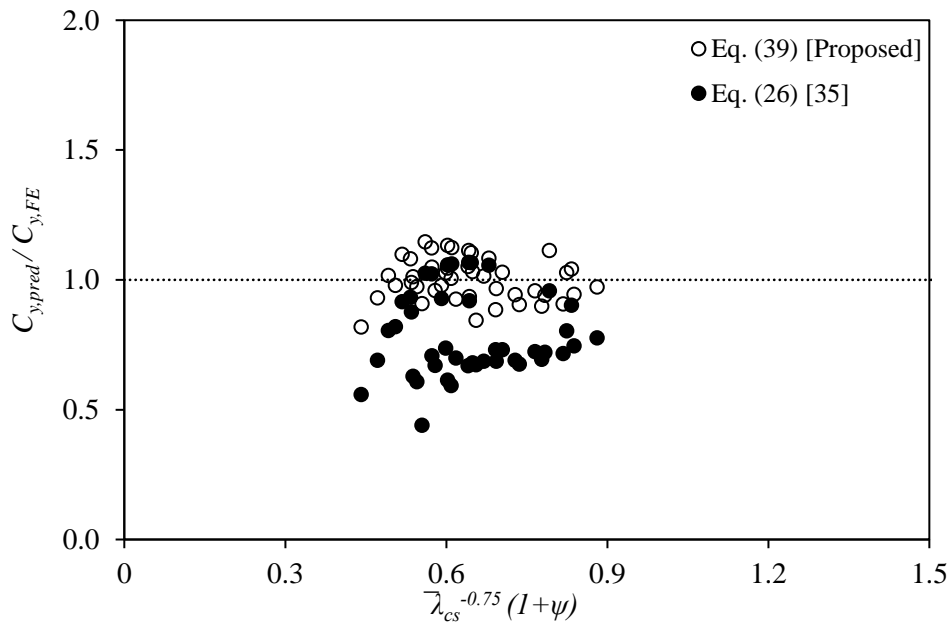
$$b_e = [0.55(1 + \psi) \bar{\lambda}_{cs}^{-0.75} + 0.15\psi] b \leq b_c \quad (40)$$

473

474



a) Calibrated C_y



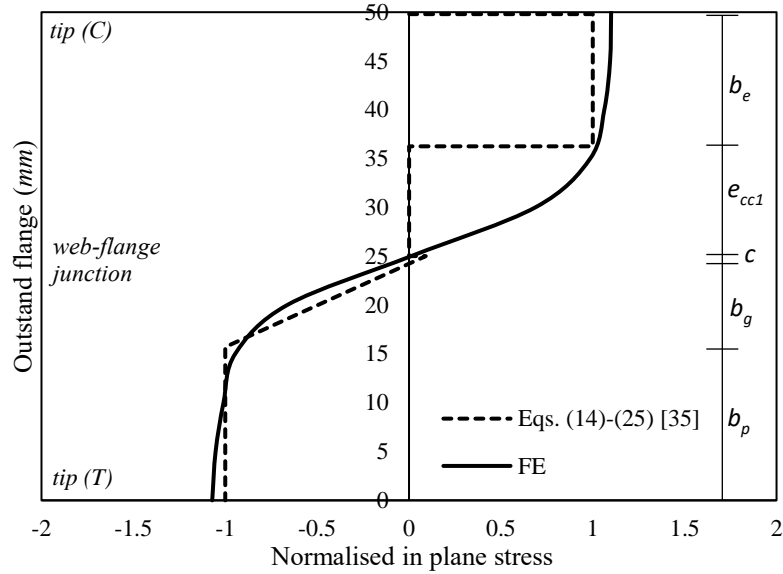
b) Comparison between Eq. (26) [35] and Eq. (39) [Proposed]

475

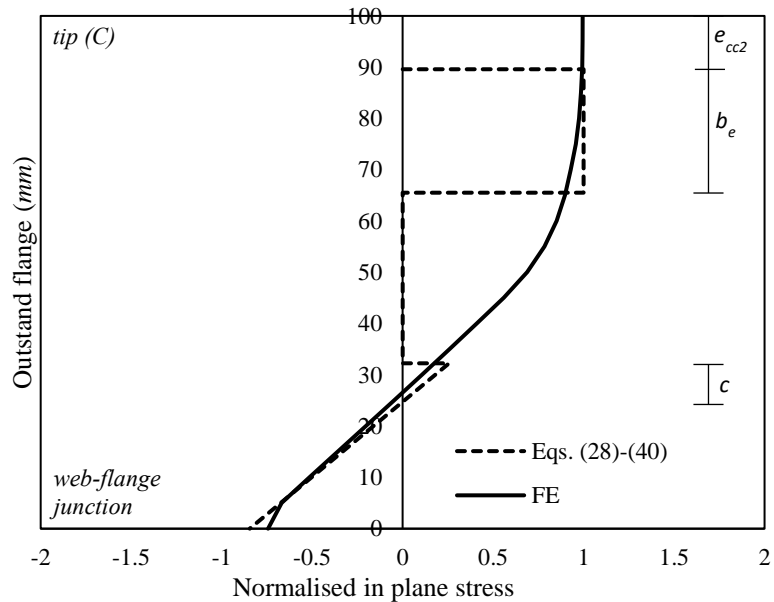
476

Figure 16: Proposed plastic effective width for C-sections - C_y coefficient based on FE data

477



a) Ferritic I-section, $100 \times 50 \times 1.5$ - $h/b=2$, $c_f/(t_f \epsilon)=19.3$, $\bar{\lambda}_{cs}=0.67$



b) Ferritic C-section, $100 \times 100 \times 2.5$ - $h/b=1$, $c_f/(t_f \epsilon)=23.3$, $\bar{\lambda}_{cs}=0.75$

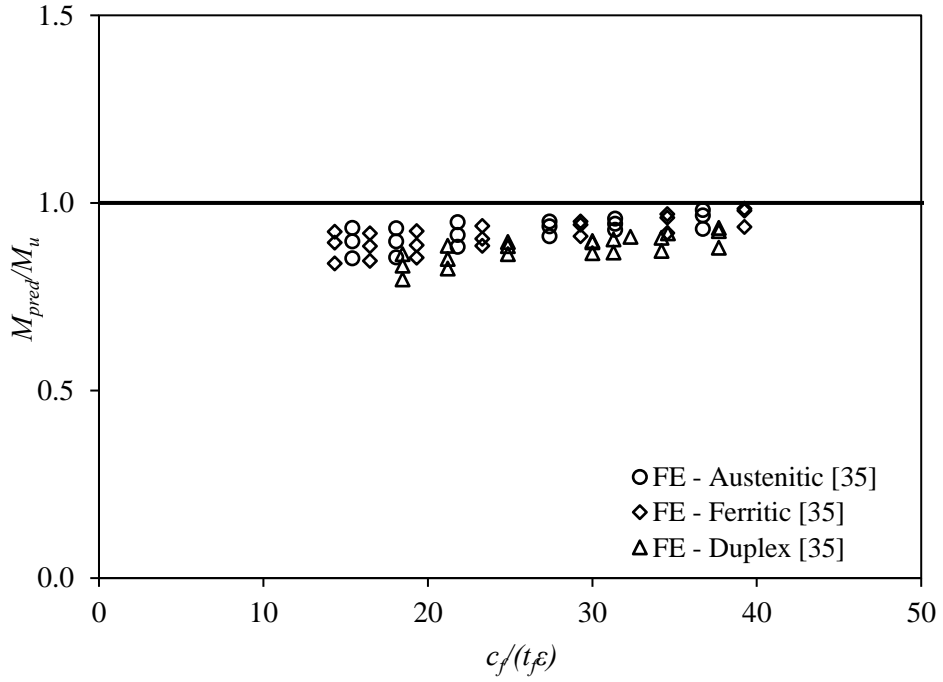
478

479

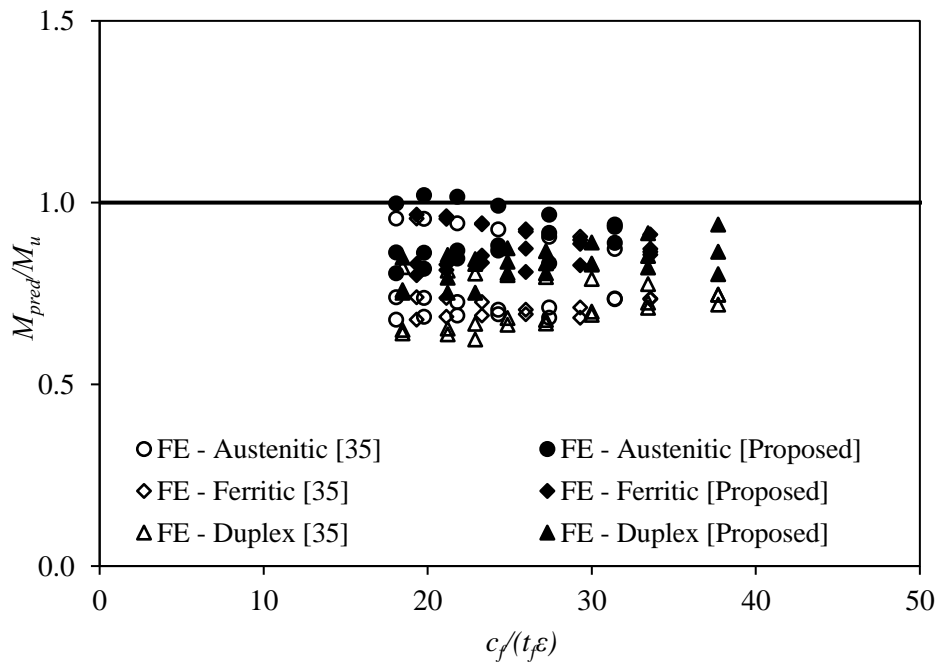
Figure 17: Comparison between FE and calculated stress distributions.

480

481 The applicability of this method is assessed in Figure 18, where the predicted-to-numerical
 482 moment resistance ratios are plotted against the slenderness parameter. The results show that
 483 Bambach et al. [35] method predicts accurately and with a high degree of consistency the
 484 bending capacities of the I-sections throughout the slenderness range considered. The proposed
 485 equations for C-sections are also assessed in Figure 18 (b) showing improved accuracy
 486 compared to those suggested at [35] (i.e. substituting Eqs. (26)-(27) with (39)-(40)). Overall, it
 487 is concluded that the improved accuracy of the predictions obtained with the plastic effective
 488 method is attributed to the rational account of the nonlinear stress distribution exhibited by
 489 locally buckled flanges.



a) I-sections: Eqs. (14)-(25)



b) C-sections: Eqs (26)-(38) [35] vs Eqs. (38)-(40) [Proposed]

490
491
492
493

Figure 18: Assessment of Plastic Effective Width Method based on FE results for Class 4 sections.

494 **4.6 Comparison of design approaches**

495 This section quantifies the accuracy of the various design approaches previously discussed in
 496 Sections 4.2-4.5. The M_{pred}/M_u ratios based on all FE results are shown in Tables 5 and 6 for I-
 497 and C-sections, respectively, thus allowing a direct comparison of all examined design methods.
 498 The tables also present the results separately for stocky and slender cross-sections, where
 499 applicable. The Eurocode predictions are overly conservative underestimating the ultimate
 500 bending capacity by approximately 43% and 39% for I-sections and C-sections, respectively.
 501 The lack of accuracy is more pronounced for slender sections, denoting average M_{pred}/M_u value
 502 as low as 0.51 for C-sections. DSM appears conservative for both slender and stocky sections.
 503 For stocky sections, the CSM provides more accurate bending capacity predictions for both I-
 504 and C-sections with M_{pred}/M_u equal to 0.80 and 0.91 respectively. Its accuracy decreases for
 505 slender sections the strength of which is largely underestimated. The plastic stress distribution
 506 of the buckled flanges of slender sections are accurately captured by the plastic effective with
 507 method, which results in a M_u/M_{pred} ratio equal to 0.91 and a COV of 0.05 for I-sections, clearly
 508 outperforming all other design approaches. For C-sections, the same method results in a
 509 M_u/M_{pred} equal to 0.74, whereas the proposed equations are capable of improving further the
 510 design accuracy to 0.87 with a significant improvement of the COV to 0.07, the smallest among
 511 all methods considered.

512

513

514 Table 5: Assessment of predicted strengths - I-sections.

	M_{pred}/M_u											
	Austenitic			Ferritic			Duplex			All		
	No FE	Mean	COV	No FE	Mean	COV	No FE	Mean	COV	No FE	Mean	COV
Stocky only												
EN 1993-1-4 (Classes 1-3)	12	0.66	0.18	9	0.65	0.19	9	0.65	0.17	30	0.65	0.17
CSM ($\bar{\lambda}_{cs} \leq 0.68$)	17	0.83	0.06	16	0.78	0.09	11	0.78	0.08	44	0.80	0.08
DSM ($\bar{\lambda}_{cs} \leq 0.474$)	10	0.61	0.06	9	0.53	0.11	9	0.51	0.05	28	0.55	0.11
Slender only												
EN 1993-1-4 (Class 4)	18	0.58	0.04	21	0.55	0.04	21	0.47	0.03	60	0.53	0.10
CSM ($\bar{\lambda}_{cs} > 0.68$)	13	0.65	0.07	14	0.64	0.08	19	0.61	0.07	46	0.63	0.08
DSM ($\bar{\lambda}_{cs} > 0.474$)	20	0.61	0.04	21	0.60	0.04	21	0.58	0.04	62	0.60	0.05
Plastic effective width [35] (Class 4)	18	0.92	0.04	21	0.92	0.05	21	0.88	0.04	60	0.91	0.05
All												
EN 1993-1-4 (All)	30	0.61	0.14	30	0.581	0.14	30	0.52	0.19	90	0.57	0.17
CSM (All)	30	0.75	0.14	30	0.71	0.13	30	0.67	0.15	90	0.71	0.14
DSM (All)	30	0.61	0.05	30	0.58	0.09	30	0.56	0.18	90	0.58	0.08

515

516

517

518
519

Table 6: Assessment of predicted strengths - C-sections.

	M_{pred}/M_u											
	Austenitic			Ferritic			Duplex			All		
	No FE	Mean	COV	No FE	Mean	COV	No FE	Mean	COV	No FE	Mean	COV
Stocky only												
EN 1993-1-4 (Classes 1-3)	12	0.81	0.22	12	0.79	0.24	6	0.77	0.26	30	0.79	0.23
CSM ($\bar{\lambda}_{cs} \leq 0.68$)	18	0.96	0.07	18	0.91	0.11	12	0.82	0.11	48	0.91	0.10
DSM ($\bar{\lambda}_{cs} \leq 0.474$)	9	0.62	0.06	9	0.59	0.06	3	0.52	0.03	21	0.59	0.09
Slender only												
EN 1993-1-4 (Class 4)	18	0.56	0.18	18	0.57	0.15	24	0.49	0.15	60	0.51	0.17
CSM ($\bar{\lambda}_{cs} > 0.68$)	12	0.81	0.10	12	0.80	0.08	18	0.80	0.09	42	0.80	0.09
DSM ($\bar{\lambda}_{cs} > 0.474$)	21	0.69	0.13	21	0.69	0.13	27	0.68	0.17	69	0.69	0.14
Plastic effective width [35] (Class 4)	18	0.78	0.14	18	0.75	0.12	24	0.71	0.09	60	0.74	0.12
Proposed method (Class 4)	18	0.91	0.08	18	0.87	0.06	24	0.83	0.06	60	0.87	0.07
All												
EN 1993-1-4 (All)	30	0.66	0.28	30	0.62	0.31	30	0.54	0.29	90	0.61	0.30
CSM (All)	30	0.91	0.11	30	0.87	0.12	30	0.80	0.10	90	0.86	0.12
DSM (All)	30	0.67	0.10	30	0.66	0.16	30	0.67	0.18	90	0.66	0.15

520 **5 CONCLUSIONS**

521 The present numerical study focussed on I- and C-sections with outstand flanges under stress
522 gradient and tip in compression. A numerical model has been developed and validated against
523 test data extracted from the literature on stainless steel sections. A total of 180 numerical results
524 considering various stainless steel grades were generated. Complementing the current structural
525 performance data on austenitic stainless steel I- and C- sections in minor axis bending, a
526 comprehensive study covering also duplex and ferritic steels was presented. The FE results
527 were used to assess design predictions. The current Eurocode Class 3 limits for outstand
528 elements in bending appear to be overly conservative for both I- and C- sections and can be
529 significantly relaxed and could be relaxed, as cross-sections with flange slenderness limits as
530 high as 40 and 30 for I- and C-sections, respectively, are still able to develop their elastic
531 moment resistance. Moreover, the bending capacity predictions of EN 1993-1-4 underestimate
532 the numerical bending resistance of I-sections by 43% on average. The source of the
533 conservatism is different for stocky and for slender sections. For stocky sections, the CSM
534 provides more accurate bending capacity predictions for both I- and C-sections with M_{pred}/M_u
535 equal to 0.80 and 0.91, respectively. The applicability of the DSM was assessed, leading to
536 conservative predictions. On the basis of the FE stress distribution, it was demonstrated that the
537 slender I- and C-sections in bending exhibit a nonlinear stress distribution in the outstand
538 elements, even when they fail prior to the attainment of their elastic moment resistance. The
539 lack of consideration of this effect is the main reason why the current codes generally provide
540 conservative and fundamentally incorrect design predictions in the slender range. To address
541 this, the plastic effective method proposed by Bambach et al. [35] for hot-rolled and cold-
542 formed steel sections subjected to minor axis bending was adapted to stainless I-sections and
543 was shown to accurately predict the numerical bending resistance with M_{pred}/M_u equal to 0.91

544 and high level of design consistency. On the basis of the FE results, new equations were
545 proposed to capture the plastic effective width of slender C-sections under minor axis bending.
546 The equations improved the accuracy of the previously suggested formulae [35] by 13% and
547 almost halved the corresponding COV. It is recommended that design guidance for slender
548 sections containing stainless steel outstand elements in bending be based on plastic effective
549 widths instead of elastic effective widths, as it was shown that the underlying principles for
550 these methods, namely the assumed stress distribution at failure, is not in agreement with the
551 observed flexural behaviour of the cross-sections.

552 REFERENCES

- 553 1. Gardner, L. and Theofanous, M., 2008. Discrete and continuous treatment of local buckling
554 in stainless steel elements. *Journal of Constructional Steel Research*, 64(11), pp.1207-1216.
- 555 2. Bock, M., Gardner, L. and Real, E., 2015. Material and local buckling response of ferritic
556 stainless steel sections. *Thin-Walled Structures*, 89, pp.131-141
- 557 3. Theofanous, M. and Gardner, L., 2009. Testing and numerical modelling of lean duplex
558 stainless steel hollow section columns. *Engineering Structures*, 31(12), pp.3047-3058.
- 559 4. Theofanous, M., Chan, T.M. and Gardner, L., 2009. Structural response of stainless steel
560 oval hollow section compression members. *Engineering Structures*, 31(4), pp.922-934.
- 561 5. Theofanous, M. and Gardner, L., 2010. Experimental and numerical studies of lean duplex
562 stainless steel beams. *Journal of Constructional Steel Research*, 66(6), pp.816-825.
- 563 6. Theofanous, M., Chan, T.M. and Gardner, L., 2009. Flexural behaviour of stainless steel
564 oval hollow sections. *Thin-Walled Structures*, 47(6-7), pp.776-787.
- 565 7. Theofanous, M., Saliba, N., Zhao, O. and Gardner, L., 2014. Ultimate response of stainless
566 steel continuous beams. *Thin-Walled Structures*, 83, pp.115-127.
- 567 8. Gkantou, M., Kokosis, G., Theofanous, M. and Dirar, S., 2019. Plastic design of stainless
568 steel continuous beams. *Journal of Constructional Steel Research*, 152, pp.68-80.
- 569 9. Arrayago, I., Real, E. and Mirambell, E., 2016. Experimental study on ferritic stainless steel
570 RHS and SHS beam-columns. *Thin-walled structures*, 100, pp.93-104.
- 571 10. Arrayago, I., Rasmussen, K.J. and Real, E., 2017. Full slenderness range DSM approach
572 for stainless steel hollow cross-section columns and beam-columns. *Journal of*
573 *Constructional Steel Research*, 138, pp.246-263.
- 574 11. Gardner, L., Bu, Y. and Theofanous, M., 2016. Laser-welded stainless steel I-sections:
575 Residual stress measurements and column buckling tests. *Engineering Structures*, 127,
576 pp.536-548.
- 577 12. Saliba, N. and Gardner, L., 2013. Cross-section stability of lean duplex stainless steel
578 welded I-sections. *Journal of Constructional Steel Research*, 80, pp.1-14.
- 579 13. Bu, Y. and Gardner, L., 2018. Local stability of laser-welded stainless steel I-sections in
580 bending. *Journal of Constructional Steel Research*, 148, pp.49-64.
- 581 14. Theofanous, M., Liew, A. and Gardner, L., 2015. Experimental study of stainless steel
582 angles and channels in bending. In *Structures* (Vol. 4, pp. 80-90). Elsevier.
- 583 15. Liang, Y., Zhao, O., Long, Y.L. and Gardner, L., 2019. Stainless steel channel sections
584 under combined compression and minor axis bending–Part 1: Experimental study and
585 numerical modelling. *Journal of Constructional Steel Research*, 152, pp.154-161.

- 586 16. Liang, Y., Zhao, O., Long, Y.L. and Gardner, L., 2019. Stainless steel channel sections
587 under combined compression and minor axis bending—Part 2: Parametric studies and
588 design. *Journal of Constructional Steel Research*, 152, pp.162-172.
- 589 17. Afshan, S., Zhao, O. and Gardner, L., 2019. Standardised material properties for numerical
590 parametric studies of stainless steel structures and buckling curves for tubular columns.
591 *Journal of Constructional Steel Research*, 152, pp.2-11.
- 592 18. Karlsson Hibbitt, Sorensen, Inc. ABAQUS. ABAQUS/Standard User's Manual Volumes I-
593 III and ABAQUS CAE Manual, 2016. Pawtucket (USA), Version 2016.
- 594 19. Gardner, L. and Nethercot, D.A., 2004. Experiments on stainless steel hollow sections—
595 Part 1: Material and cross-sectional behaviour. *Journal of Constructional Steel Research*,
596 60(9), pp.1291-1318.
- 597 20. EN 1993-1-4:2006+A1:2015. Eurocode 3: design of steel structures – part 1. 4: general
598 rules – supplementary rules for stainless steels, including amendment A1 (2015). Brussels:
599 European Committee for Standardization (CEN); 2015.
- 600 21. EN 1993-1-5. Eurocode 3: Design of steel structures – Part 1. 5: Plated structural elements.
601 Brussels: European Committee for Standardization (CEN); 2006.
- 602 22. Zhang, L., Wang, F., Liang, Y. and Zhao, O., 2020. Experimental and numerical studies of
603 press-braked S690 high strength steel channel section beams. *Thin-Walled Structures*, 148,
604 p.106499.
- 605 23. Wang, F., Zhao, O. and Young, B., 2019. Flexural behaviour and strengths of press-braked
606 S960 ultra-high strength steel channel section beams. *Engineering Structures*, 200,
607 p.109735.
- 608 24. Sun, Y., He, A., Liang, Y. and Zhao, O., 2019. In-plane bending behaviour and capacities
609 of S690 high strength steel welded I-section beams. *Journal of Constructional Steel*
610 *Research*, 162, p.105741.
- 611 25. Afshan, S. and Gardner, L., 2013. The continuous strength method for structural stainless
612 steel design. *Thin-Walled Structures*, 68, pp.42-49.
- 613 26. Zhao, O., Afshan, S. and Gardner, L., 2017. Structural response and continuous strength
614 method design of slender stainless steel cross-sections. *Engineering Structures*, 140, pp.14-
615 25.
- 616 27. Zhao, O. and Gardner, L., 2018. The continuous strength method for the design of mono-
617 symmetric and asymmetric stainless steel cross-sections in bending. *Journal of*
618 *Constructional Steel Research*, 150, pp.141-152.
- 619 28. Seif, M. and Schafer, B.W., 2010. Local buckling of structural steel shapes. *Journal of*
620 *Constructional Steel Research*, 66(10), pp.1232-1247.
- 621 29. Gardner, L., Fieber, A. and Macorini, L., 2019, February. Formulae for calculating elastic
622 local buckling stresses of full structural cross-sections. In *Structures* (Vol. 17, pp. 2-20).
623 Elsevier.
- 624 30. Schafer BW, Peköz T. Direct strength prediction of cold-formed steel members using
625 numerical elastic buckling solutions. In: *Proceedings of the Fourteenth International*
626 *speciality conference on cold-formed steel structures*. St. Louis (MO, USA); 1998.
- 627 31. Schafer, B.W., 2008. The direct strength method of cold-formed steel member design.
628 *Journal of constructional steel research*, 64(7-8), pp.766-778.

- 629 32. Becque, J., Lecce, M. and Rasmussen, K.J., 2008. The direct strength method for stainless
630 steel compression members. *Journal of Constructional Steel Research*, 64(11), pp.1231-
631 1238
- 632 33. Rossi, B. and Rasmussen, K.J., 2013. Carrying capacity of stainless steel columns in the
633 low slenderness range. *Journal of Structural Engineering*, 139(6), pp.1088-1092.
- 634 34. Arrayago, I., Rasmussen, K.J. and Real, E., 2017. Full slenderness range DSM approach
635 for stainless steel hollow cross-sections. *Journal of Constructional Steel Research*, 133,
636 pp.156-166.
- 637 35. Bambach, M.R., Rasmussen, K.J. and Ungureanu, V., 2007. Inelastic behaviour and design
638 of slender I-sections in minor axis bending. *Journal of Constructional Steel Research*, 63(1),
639 pp.1-12.